JPRS-CST-94-003
3 MARCH 1994

FOREIGN
BROADCAST
INFORMATION
SERVICE

JPRS Report

Science & Technology

China

NANOMATERIALS

JPRS-CST-94-003
3 MARCH 1994

SCIENCE & TECHNOLOGY

CHINA
NANOMATERIALS

CONTENTS

Ion Conductivity in Nanoscale $Ca_{1-x}La_xF_{2+x}$

93P60207A Beijing KEXUE TONGBAO [CHINESE SCIENCE BULLETIN] in Chinese Vol 38 No 3, 1-15 Feb 93 pp 221-223

[Article by Su Fang [5685 2499] and Xie Bin [6200 2430] of the University of Science and Technology of China Basic Physics Center, Structural Analysis Open Laboratory, Hefei 230026, and Wu Xijun [0702 1585 0193] and Qin Xiaoying [4440 2556 5391] of the CAS Institute of Solid State Physics, Hefei 230031: "Ion Conductivity in Nanometer $Ca_{1-x}La_xF_{2+x}$"; supported by grants from NSFC and State High-Tech [863] Plan New Materials Area; MS received 7 Jul 92, revised 16 Oct 92]

[Abstract] Via an inert gas evaporation and vacuum in-situ pressurization/vacuum deposition technique, the authors have prepared two bulk nanoscale materials exhibiting fluorine ion conductivity—CaF_2 and $Ca_{0.75}La_{0.25}F_{2.25}$—the first report worldwide of F ion conductivity in nanoscale materials. The CaF_2 material has very uniform ultrafine particles with a granularity of 10-20 nm (average 15 nm). Measurements indicate that the nanoscale CaF_2 ion conductivity is higher than that of polycrystalline CaF_2 by 1 order of magnitude (at 300°C) or 0.8 order of magnitude (at 530°C), and 2 orders of magnitude higher than that of monocrystalline CaF_2; ion conductivity activation energy is 1.13 eV. For the nanoscale $Ca_{0.75}La_{0.25}F_{2.25}$ material, ion conductivity measures 1 order of magnitude (at 300°C) or 0.6 order of magnitude (at 530°C) higher than that for the nanoscale CaF_2; ion conductivity activation energy is 0.997 eV. Figure 1 (not reproduced) shows a TEM photograph of the material granularity while Figures 2 and 3 (not reproduced) depict various graphs of the measured data.

References

1. Reau, J. M., Lucat, C., Campet, G. et al., J. SOLID STATE CHEM., 1976, 17: 123-129.

2. Lucat, C., Campet, G., Claverie, J. et al., MAT. RES. BULL., 1976, 11: 162-172.

3. Su Fang, SOLID STATE IONICS, 1982, 7: 37-41.

4. Su Fang, Xu Wei, Su Jun, WULI XUEBAO [ACTA PHYSICA SINICA], 1991, 40(4): 596-603.

Research on Nanoscale Direct Etching on Graphite Surface

93FE0753A Beijing KEXUE TONGBAO [CHINESE SCIENCE BULLETIN] in Chinese Vol 38 No 5, 1-15 Mar 93 pp 433-435

[Article by Wang Zhonghuai [3769 1813 2037], Dai Changchun [2071 7022 2504], Sun Hong [1327 4767], and Bai Chunli [4101 2504 4409, liaison person] of the Institute of Chemistry, Chinese Academy of Sciences, Beijing 100080: "Study of Nanoscale Direct Etching on Graphite Surface"; funded by the Natural Science Foundation of China and the Chinese Academy of Sciences; MS received 4 Sep 92, revised 15 Nov 92. Cf. brief report in JPRS-CST-92-017, 24 Sep 92 p 25]

[Text] The utilization of scanning tunneling microscope (STM) to nanoscale process the surface of a conductor or a semiconductor can theoretically further understanding of atom or molecule movement rules as well as basic research on mesoscopic physics, quantum mechanics, etc. This use also has the potential for application in areas such as manufacturing of high-density information storage components, nanoscale electronic components, etc. Recently, some progress has been accomplished in the field.[1] (Footnote 1) (Ma Zili, Shen Jian, Zhu Changxin et al., Proceedings of First National Conference on Nanoscale Science and Technology (in printing).) Using the institute's independently developed STM,[2] we directly etched different Chinese characters and designs on graphite surfaces by applying pulse voltage between the probe and the specimen.

1. Experimental Method

The experiment instrument is the independently made Model CSTM-9000 STM[2] operated in atmosphere. A computer controls the probe pulse voltage. The probe can be positioned precisely anywhere in the scanning area. The 0.25-mm-diameter probe is made of 80Pt-20Ir alloy by mechanical shearing. The base material is high-orientation cleavaged graphite.

Graphite surface etching is processed in two steps: First the computer controls the probe in a tunneling state to move or to position along a predetermined path. At the specific location, the computer applies a pulse voltage between the probe and the specimen. Thus, physical and chemical reactions occur at the location to produce the mark. The second step is continuously moving the probe to etch a design on the graphite surface. In order to assure that there is no contact between the probe and the specimen during etching, the feed-back is not shut off.

Instead of using the experimental parameters of Albrecht et al.,[1] we adopted a 3-6 V pulse amplitude to write characters and etch designs. The pulse width is between a few tenths to ten-odd milliseconds. Constant-current mode is used throughout the experiment.

2. Results and Discussions

Figure 1 shows the structures of three predetermined etched locations formed by pulse voltage on the graphite surface. The structures of both bumps and cavities appear at each location. The scanning range is 82 nm x 97 nm. The similarities of the general structures of these three spots indicate that the probe shape affects the etched marking.

Figure 1. Pulse Voltages Are Applied on Three Defined Locations and Form Three Similar Rough Structures (scanning area: 82 nm x 97 nm)

Figure 2 shows the characters and designs with 10 nm line width which are control-etched by the computer software. Figure 2(a) shows the two characters "Zhong Guo," each character having a size of 200 nm x 200 nm. The scratch mark in Figure 2(a) is caused by the probe or the surface physical or chemical reactions while they are still in an unstable condition after etching. The graph generally becomes sharper after repeated operations. Figure 2(b) shows the English letters "CAS" (the abbreviation of Chinese Academy of Sciences). Each letter is the size of a 60 nm square. In Figure 2(b), it seems that the lines are formed by removing one or more layers of graphite atoms from the local region under the probe. It is also possible that lines are formed by chemical reactions which alter the electronic state.

Figure 2. Characters and Designs With Line Width About 10 nm Etched With a Pulse Voltage Amplitude of About -4.5 V and Width of 8 ms. (a) The two etched characters "Zhong Guo," character size: 200 nm x 200 nm. (b) The English letters "CAS," letter size: 60 nm x 60 nm

The following phenomena in this experiment have been observed: (1) There is a threshold amplitude value (generally about -3 V) for the pulse voltage to produce an observable reaction between the probe and the specimen. This threshold value is related to the probe's condition (including its shape). In addition, the changing of the pulse width affects the test results more. The probe shape and the pulse width determine the line width. (2) After the completion of the etching process, the probe is still in good condition, and still reaches an atomic-level resolution. It is possible that the etching process actually further ameliorates the probe. (3) The surface graphite of the etched region becomes quite loose because of the laminated structure of high-orientation graphite. After a period of repeated scannings, the structure easily becomes random. This observation is the same as that of Albrecht et al.[1] (4) Probe condition (including its shape) crucially affects etching results. Under the same conditions, including base material, pulse (amplitude and width) and other experimental parameters as well as even probe material, the etching results are not necessarily the same. The experimental results show that bumps and cavities appear simultaneously. (5) The experiment encountered quite a few multi-probe effects.[3] We presume that the effect is shown by two features as follows: First, during etching, the multi-probes react and form many probe marks on the surface; and second, the etching marks have heavier undulations contributed by the multi-probes.

The STM has been used frequently for surface decoration, etching and writing; however, researchers differ on the explanations of its etching mechanism. Because experimental works are not sufficiently in depth, research on the mechanism is still inconclusive in many areas. The purpose of studying the mechanism is to produce lines and patterns that are more uniform, finer, and tolerant of repetitive etching. We believe that the possible mechanisms of graphite surface etching are as follows: (1) Due to long pulse time, and high local energy density, as well as the possibility of contamination of the probe in the atmosphere, sufficient energy is produced causing the deposition of probe contamination on the graphic surface. (2) Local high energy density probably can heat up the atoms in the local region and thus evaporates them.[4] Calculations[1] indicate that continuous pulse voltage can only increase surface temperature by no more than 5°C. However, the calculation is based on macroscopic observation, and it may be unsuitable for the STM's nanoscale operation. (3) The nanoscale beam current supplied by the STM probe induces some chemical reactions between the surface carbon or other atoms adsorbed from air, or even the surface substances. Consequently, these reactions produce a different topography or a change of the electronic state within the microscopic region under the probe. Since the STM image contains information on the electronic state and topography, the moving of the probe will display a mark on the STM image. As to the occurrence of bumps and cavities, our explanations are as follows: Because the graphite surface is fairly flat, the single atom at the tip of the probe contributes the most to the tunneling current for the formation of the atomic image. However, in etching, the probe provides a closed electric field; therefore, the reaction spot is not a single atom, but a nm area of the probe tip. The probe has a complicated form, and a macroscopically very sharp tip is still very rough in nanoscale. Moreover, between the probe and the surface, there are many physical quantities, such as energy density, electrical field, beam current, etc., which are subject to the influence of the form of the probe tip. The material from the rough probe will deposit a similar mass of material on the surface. It is also possible that varying degrees of chemical reactions occur between the nm-scale region on the probe and the micro-region on the surface and thus evaporate the material at varying rates. Consequently, the complicated probe topography results in the complicated mark topography. Actually the topography of a mark is an indirect reflection of the probe.

3. Conclusions

Based on the experiments, we conclude:

(1) It is possible to write or to etch designs on the graphite surface by computer control of a pulse of -3 to -6 V in amplitude and a few ms to ten-odd ms in width. The process is repeatable.

(2) There is a threshold pulse voltage (about -3 V) to produce an observable reaction between the Pt/Ir probe and the graphite specimen.

(3) In the etching experiment, the probe shape has a critical effect. The shape affects not only the threshold pulse voltage, but also the topography of the mark.

Acknowledgment

The authors are grateful for assistance from the comrades in the STM Section, Shanghai Institute of Nuclear Research, Chinese Academy of Sciences.

References

1. Albrecht, T. R., Dovek, M. M., Kirk, M. D., et al., APPL. PHYS. LETT., 1989, 55 (17): 1717-1729.

2. Bai Chunli, KEXUE TONGBAO [CHINESE SCIENCE BULLETIN], 1989, 34 (5): 339-340.

3. Hu, J., Gu, M. M., Wang, Z. H., et al., JPN. J. APPL. PHYS., 1992, 31 (1): 110-113.

4. Li, Y. Z., Vazquez, L., Piner, R., et al., APPL. PHYS. LETT., 1989, 54 (15): 1424-1426.

Reports on Fabrication, Characterization of Nanoparticles

ZnO Nanocrystalline Sensitive Material

93P60293A Changchun JILIN DAXUE ZIRAN KEXUE XUEBAO [ACTA SCIENTIARUM NATURALIUM UNIVERSITATIS JILINENSIS] in Chinese No 2, May 93 pp 116-118

[Article by Zhang Lihua [1728 7787 5478], Wang Zichen [3769 1311 1820] et al. of the Dept. of Chemistry, Jilin University, Changchun 130023: "Preparation of Zinc-Oxide Nanocrystalline Sensitive Material"; MS received 4 Oct 92, supported by grant from NSFC]

[Abstract] Via a citrate method—domestically manufactured $Zn(NO_3)_2.6H_2O$ dissolved in citric acid and imported (from Japan) polyethylene glycol—nanoscale polycrystalline ZnO particles of diameter 20 nm, 26 nm, and 31 nm (processing at 450, 500, and 550°C, respectively) have been synthesized. Instruments used include a Shimadzu Corp. model XD-3A X-ray diffractometer, a Hitachi model H-800EM electro-optical TEM, a PE (U.S. company) model DTA 1700 differential thermal analyzer, and a Nicolet Instruments Corp. (U.S. firm) model 5 DX infrared absorption spectrometer. The effects of heating temperature and heating time in the course of crystallization are studied. The nanoparticles prepared are high-purity, uniform, spherical, cubic polycrystals.

Four figures, no tables.

References

1. Seiyama, T., et al., ANAL. CHEM., 1962; 34: 1502.
2. Seiyama Kagaula, T., ANAL. CHEM., 1966; 1070: 38.
3. Zeng Hengxing, CAILIAO KEXUE JINZHAN [ADVANCES IN MATERIALS SCIENCE], 1989; 3(3): 215-219.
4. Dong Qingnian, "Hongwai Guangpu Fa" [Infrared Spectroscopic Techniques], Petrochemical Industry Publ. House, Beijing, 1977.

TiO_2 Ultrafine Particles

93P60293B Changchun JILIN DAXUE ZIRAN KEXUE XUEBAO [ACTA SCIENTIARUM NATURALIUM UNIVERSITATIS JILINENSIS] in Chinese No 2, May 93 pp 119-122

[Article by Bao Xinnu [7637 2450 0505], Zhang Yan [1728 1484], Xiao Liangzhi [5135 5328 6347], and Li Tiejin [2621 6993 3160] of the Dept. of Chemistry, Jilin University, Changchun 130023 (Xiao and Li also of the CCAST, World Lab, Beijing 100081), and Lai Zuyou [6351 4371 3731] and Gu Shiwei [7357 0013 3161] of the Dept. of Applied Physics and Institute of Condensed-Matter Physics, Shanghai Jiaotong University, Shanghai 200030: "Influence of Surface Coating on Optical Properties of TiO_2 Ultrafine Particles"; MS received 22 Aug 92, supported by grant from NSFC]

[Abstract] A series of TiO_2 ultrafine particles (UFPs) coated with a layer of oleic acid radicals have been synthesized. Preparation includes mixing titanium tetrachloride and sodium oleate in toluene, followed by a hydrolysis reaction to produce the oleic-acid-coated TiO_2 UFPs, in which the toluene sol is yellow-orange or red. Instruments used include a Rigaku model D/MAX-RA 12 kW small-angle X-ray scatterometer and a Shimadzu model UV-365 spectrophotometer. It was found that the apparent optical band gap E_g decreases and the red shift of optical absorption band edge increases when the particle diameter d decreases. Table 1 gives the following values of diameter and apparent optical band gap for samples 1-5 (samples 1-3 are coated, samples 4-5 are uncoated), respectively: 3.68 nm, 2.84 eV; 3.55 nm; 2.71 eV; 3.30 nm, 2.41 eV; 4.36 nm, 3.69 eV; 2.93 nm, 3.74 eV. Table 2 shows that for particles of same d (3.55-3.56 nm), E_g for the oleic-acid-coated TiO_2 UFPs is similar to that of stearic-acid-coated TiO_2 UFPs (2.71 eV vs. 2.63 eV), but bigger than the E_g (2.46 eV) of TiO_2 UFPs coated with dodecylbenzene sulfonic acid (DBS).

Two figures.

References

1. Gratzel, M., "Energy Resources Through Photochemistry and Photocatalysis," Academic Press, 1983.
2. Brus, L. E., J. PHYS. CHEM., 1986; 90: 2555.
3. Zou Bingsuo et al., JILIN DAXUE ZIRAN KEXUE XUEBAO, 1990; (4): 117.
4. Zou Bingsuo et al., APPL. PHYS. LETT., 1991; 59(15): 1826.
5. Huang Shengtao, ed., "Structure and Structural Analysis of Amorphous Materials," Science Publ. House, Beijing, 1987: 142.
6. Tauc, J., "Optical Properties of Solids," North-Holland, Amsterdam, 1970; 279.
7. Anpo, M., et al., J. PHYS. CHEM., 1987; 91: 4305.
8. Michael, L., et al., ACC. CHEM. RES., 1990; 23: 183.

Kinetic Model for Initial Sintering Stage of Y-TZP Nanoscale Powder

93FE0761A Beijing GUISUANYAN XUEBAO [JOURNAL OF THE CHINESE CERAMICS SOCIETY] in Chinese Vol 21 No 1, Feb 93 pp 29-32

[Article by Xu Yueping [1776 6490 5493] (correspondent, Shanghai Institute of Ceramics, Chinese Academy of Sciences, Shanghai, 200050), Guo Jingkun [6753 2529 0981], Ma Litai [7456 0448 3141], and Ruan Meiling [7086 5019 3781] of the Shanghai Institute of Ceramics, Chinese Academy of Sciences: "Study of Kinetic Model for Initial Sintering Stage of Y-TZP Nanoscale Powder"; MS received 22 Jul 91]

[Excerpts] **Abstract**

Based on the kinetics study of the initial stage of sintering of Y-TZP nanoscale powder, it is found that grain boundary expansion is the main cause of shrinkage in the early sintering stage. The equation of the corresponding sintering kinetics is derived.

1. Foreword

Systematic sintering research aims to establish a kinetic model for the early stage of sintering. Past researchers derived many corresponding models,[1-5] and experiments prove that they were correct to a certain degree. The continuous development of superfine powder (SFP) science makes researchers pay more attention to the study of sintering SFPs. Through theoretical derivation and experimental verification, this paper derives a model of initial-stage sintering so that improved sintering kinetics rules can be established and used as a basis for experiment.

2. Experiment

Y-TZP SFP was made by co-precipitation, then separated by wet colloidal condensation treatment, and subsequently freeze-dried.[6] For discussion, the powder characteristics are listed in the following table:

Characteristics of Powder (700°C, 2h)

Powder	d_{BET}/nm	d_{50}/µm	d^+/nm	AF	Strength of agglomerate/MPa
3Y-TZP	22	0.82	19	37.27	45

In the table: d^+ represents the powder particle size, determined by X-ray broadening; d_{50}, the particle size at the median of weight frequency distribution; and AF = d_{50}/d_{BET}, the agglomerate constant of the agglomerate size. The agglomerate strength is determined by a series of tests to establish the relationship between the green compact density and the pressing pressure. To make the green compact, the powder is first compacted from both directions with a pressure of 200 MPa, and then compacted under a static hydraulic pressure of 300 MPa. Type 402ES-3 dilatometer was used to measure the relationship of the initial-stage compact shrinkage and the sintering time. TEM was used to study the coherency between powder particles.

Before discussing the sintering model, we assume that during sintering, the initial shrinkage stage is defined as when the linear shrinkage rate is less than 5 percent. Because of the minute particle size, the non-agglomerated SFP has large specific surface area, hence, the driving forces during sintering are greatly increased. For example: When the particle configuration is assumed to be spherical, for the 20 nm SFP, the sintering driving force is approximately as follows:

$$\Delta P = 2\gamma/R = 2 \times 0.8/10 \times 10^{-9} = 16 \times 10^7 \text{ N/m}^2,$$

where γ represents surface tension. Under this driving force, the stress in the contacting surfaces among particles is increased. [passage omitted]

4. Conclusion

Based on the mechanism of densification by sintering the Y-TZP SFP, the initial sintering stage model and the corresponding kinetic equation are derived. The model is verified by using real-time measurement of test specimens.

References

1. Coble, R. L., "Sintering Crystalline Solids II. Experimental Test of Diffusion Models in Powder Compacts," J. APPL. PHYS., 1961; 32 (5): 793.

2. Coble, R. L., "Sintering Crystalline Solids I. Intermediate and Final State Diffusion Models," J. APPL. PHYS., 1961; 32 (5): 787.

3. Johnson, W. C., Coble, R. L., "A Test of the Second Phase and Impurity Segregation Models for MgO Enhanced Densification of Sintered Alumina," J. AM. CERAM. SOC., 1978; 61 (3-4): 110.

4. Kingery, W. D., Francois, B., "Grain Growth in Porous Compacts," J. AM. CERAM. SOC., 1965; 48 (10): 546.

5. Johnson, D. L., "Solid State Sintering," In: Burke, J. J., Reed, N. L., Weiss, V., eds., "Ultrafine Grain Ceramics," Chap. 9, New York: Syracuse University Press, 1970: 173.

6. Xu Yaoping, Guo Jingkun, Huang Xiaoxian, "The Preparation and Micro-Characteristics of Non-Agglomerate ZrO_2-Y_2O_3 Superfine Powder," GUISUANYAN XUEBAO [JOURNAL OF THE CHINESE CERAMICS SOCIETY], 1991; 19 (3): 269.

7. Hashimoto, K., Hamano, T., trans. into Chinese by Chen Shixing, "Fundamentals of Ceramics," Beijing: Light Industries Press, 1984: 174.

8. Herring, C., "Effect of Change of Scale on Sintering Phenomena," J. APPL. PHYS., 1950; 21 (4): 301.

Development of High-Temperature Ceramic Composites

93FE0761C Beijing GUISUANYAN XUEBAO [JOURNAL OF THE CHINESE CERAMICS SOCIETY] in Chinese Vol 21 No 1, Feb 93 pp 77-87

[Article by Shi Keshun [0670 0668 7311], correspondent, Chinese Ceramic Society, Baiwanzhuang, Beijing 100831: "Development of High Temperature Composite Materials"; MS received 19 Jun 92]

[Excerpts] **Abstract**

Based on the requirements for applications above 1,600°C, this paper comments on the current status of high-temperature properties and limitations of structural ceramics and ceramic matrix composites (CMCs). It analyzes and discusses certain directions in high-temperature CMC development, introduces the key aspects of microcomposite and nanocomposite materials, and briefly introduces functionally gradient materials (FGMs). For applications within the temperature range of 1,204-1,371°C, attention is focused on ceramics and CMCs of reasonable cost. Currently, the most promising materials for 1,600°C and above in the atmosphere are those in the oxide/oxide system, i.e., oxide matrices reinforced with oxide fibers. At present, research on SiC/SiC, and SiC/Si_3N_4 composites is stressed. A composite made by an integrated micro- and nanocomposite technology is probably the [most promising] new concept for the development of materials with super-strength and super-toughness. [passage omitted]

3. Ceramic Nanocomposites and Functionally Gradient Materials

To find a structural material for application at temperatures above 1,600°C, nanoceramics, especially ceramic nanocomposites (CNCs), probably offer an important course to follow.[14,15] It has been proven that the room-temperature hardness and toughness of CNCs are 2 to 5 times those of monolithic ceramics. The high-temperature strength, creep resistance, fatigue failure, and thermal shock resistance of CNCs have been greatly improved. For certain special applications, such as insulation structural materials for 21st-Century aircraft and spacecraft, FGMs may be a candidate.

3.1 CNC Categories

There are two categories of CMCs: microcomposites and nanocomposites (CNCs). In microcomposites, the microscale second phases, such as particles, crystal platelets, crystal whiskers, and fibers, are dispersed along the matrix grain boundaries. The function of such a dispersion is to improve the material fracture toughness.

Nanocomposites are divided into three classes: intra-type, inter-type, and nano/nano-type, as shown in Figure 6. From Figure 6, we can see that the nanoscale particles are distributed either inside the matrix grains (intra-type) or along the matrix grain boundaries (inter-type). The purposes of these distributions are to improve not only the materials' room-temperature mechanical properties and service lives, but also their high-temperature mechanical properties, such as hardness, strength, creep resistance, and fatigue fracture resistance. The nano/nano-type materials are made of nanoscale matrix crystal grains and nanoscale dispersion phases. The nano/nano materials have additional properties, such as fabricability and super-plasticity, similar to those of metals.

3.2 CNC Properties

The earliest CNCs were made by chemical vapor deposition (CVD) technology. CVD technology is a good method for dispersing the second phase into matrix crystal grains, or along the grain boundaries.

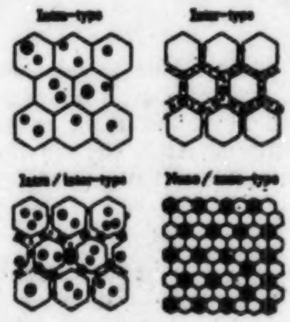

Figure 6. Classification of Ceramic Nanocomposites

However, CVD is not feasible for mass production, and it is costly. To make structural ceramics, sintering technology is more practical. Hirokazu Niibara, using the hot pressing technique (Figure 7) as well as non-pressing sintering and hot isostatic pressing (HIP) technique, successfully made CNCs such as Al_2O_3/SiC, Al_2O_3/Si_3N_4, Al_2O_3/TiC, Mullite/SiC, B_4C/SiC, B_4C/TiB_2, SiC/amorphous SiC, and Si_3N_4/SiC, etc.

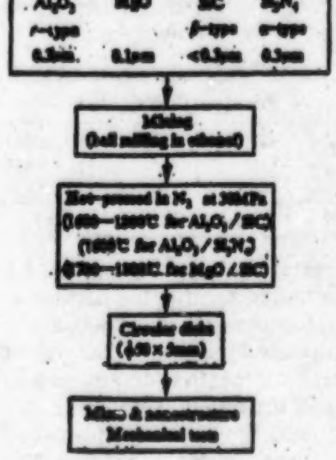

Figure 7. Fabrication Processes of Al_2O_3/SiC, Al_2O_3/Si_3N_4 and MgO/SiC Nanocomposites

Table 3 and Figures 8-12 show the CNC property improvements.

Table 3. Improvement of the Mechanical Properties Observed for the Ceramic Nanocomposites

Composite systems	Toughness K_{IC}/MPa-m$^{1/2}$	Strength σ_f/MPa	Maximum operating temperature T/°C
Al_2O_3/SiC	3.5 → 4.8	350 → 1520	800 → 1200
Al_2O_3/Si_3N_4	3.5 → 4.7	350 → 850	800 → 1300
MgO/SiC	1.2 → 4.5	340 → 700	600 → 1400
Si_3N_4/SiC	4.5 → 7.5	850 → 1550	1200 → 1400

3.2.1 When 5-volume-percent nanoscale SiC particles are dispersed in the Al_2O_3 matrix grains, the strength of the composite material is about 3 times higher than that of alumina. When the composite is annealed at 1,300°C for 1 hour in atmosphere or inert gas, its strength is further increased to 1,550 MPa (Figure 8).

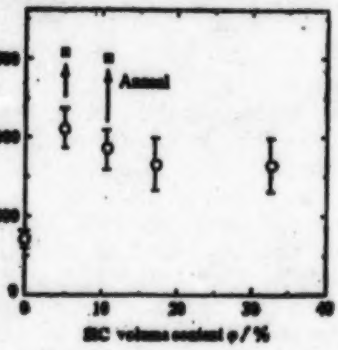

Fig. 8 Improvement of fracture strength by nano-size SiC dispersion for the Al_2O_3/SiC nanocomposites

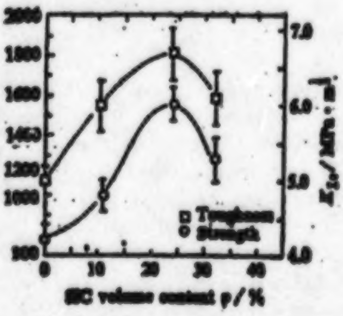

Fig. 9 Improvement of fracture toughness and strength by the nano-size SiC dispersion for the Si_3N_4/32%(vol) SiC nanocomposite

3.2.2 Si_3N_4/SiC CNC is an inter-type CNC. When the SiC content is 25 volume percent, its toughness and strength reach maximum, 6.7 MPa-m$^{1/2}$ and > 1,500 MPa, respectively (Figure 9). The degrees of increases are quite high.

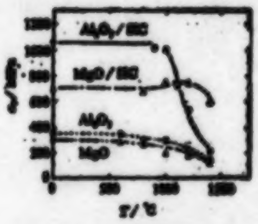

Fig. 10 Temperature dependence of the fracture strength for the Al_2O_3/5%(vol) SiC and MgO/30%(vol) SiC nanocomposites

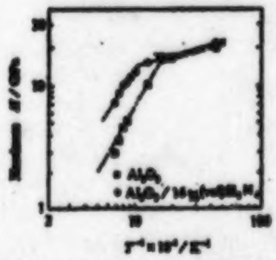

Fig. 11 Variation of Vickers hardness with temperature for the Al_2O_3/16%(vol) Si_3N_4 nanocomposite

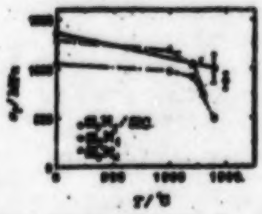

Fig. 12 Temperature dependence of fracture strength of the Si_3N_4/32%(vol) SiC nanocomposite

3.2.3 Compared with Al_2O_3 and MgO ceramics, Al_2O_3/SiC, Al_2O_3/Si_3N_4, and MgO/SiC CNCs have much improved strength at temperatures above 1,000°C (Figure 10). The high-temperature strength of MgO/SiC CNC is strikingly improved. The MgO/30-vol%SiC CNC has higher strength in the temperature range 1,000-1,400°C than at room temperature. At 1,500°C, its strength is still close to 600 MPa. From Figure 11, we can see that the CNC's transition point of hardness in reference to temperature (or brittleness to ductility transition temperature, BDTT) is higher than the transition point of monolithic Al_2O_3.

3.2.4 The flexural strength (σ_f) of Si_3N_4/SiC CNC shows no apparent decrease up to 1,400°C. The σ_f of CNC containing 32 volume percent of nanoscale SiC is still above 1,000 MPa; and is about 900 MPa at 1,500°C. In Si_3N_4/SiC CNC, the nanoscale SiC grains disperse both inside the matrix grains and along the grain boundaries, a dispersion pattern different from those of the aforementioned materials.

3.2.5 The SiC/SiC inter-type CNC made from a mixture of SiC powder and polysilastyrene sintered in argon can maintain its strength at temperatures up to 1,500°C. It also has good fabricability similar to that of metals, e.g., thread turning. It is assumed that helical carbon which acts as a lubricant during machining contributes to the fabricability.

3.3 Function of Nanoscale Dispersion Phase

The apparent mechanical property improvements of CNCs, especially oxide CNC, are due to the following reasons: (1) The nanoscale dispersed SiC or Si_3N_4 suppresses the grain growth of the oxide matrix, and inhibits the tendency of excessive grain growth. (2) Local high stresses exist within the dispersion phases and the areas around the dispersion phases. The stresses are induced by the thermal expansion difference between the matrix and the dispersion phases. During cooling, dislocations are generated. The nanoscale particles pierce into or enter the dislocation zones, forming sub-grain boundaries, resulting in the further refining of matrix grains, and consequently the reinforcing of the matrix. (3) The local tensile stress around the nanoscale particle breaks each matrix single crystal in the local area, and the reflex effect between the hard particle and the crack tip promotes local ductility. The breaking modes include intra-grain, or inter-grain, or single-crystal cracking. The changes of grain boundary phases (amorphous phase, almost 10 volume percent of total), which decrease the boundary influence on the high-temperature mechanical properties, significantly improve the high-temperature mechanical properties of the material. (4) The nanoscale SiC particles inhibit the dislocation movement. Consequently, the high-temperature mechanical properties such as hardness, strength, and creep resistance are improved. The improvement of these properties also improves the thermal shock and other thermal mechanical properties.

The function of dispersion phase in Si_3N_4/SiC CNC is obviously different from that in oxide CNC in the following three aspects: (1) When the SiC content is low, during sintering, the nanoscale SiC particles form nuclei for the precipitation of β-Si_3N_4, thus stimulate the growth of fine, slender, and uniformly distributed β-Si_3N_4. This type of grain structure increases material strength and toughness. (2) When the SiC content is high (> 25 percent), the dispersion phase prevents the growth of slender Si_3N_4 grains. Eventually, fine equiaxial Si_3N_4 grains are formed and the material becomes nano/nano-type composite. This type of material has super-plasticity at high temperatures. (3) Nanoscale SiC particles exist along the Si_3N_4 grain boundaries. Although 8 weight percent of Y_2O_3 is added as a sintering booster, impurity phase is not observed between the grain boundaries of SiC and Si_3N_4. This indicates that the dispersion phase and the matrix are directly bonded, which improves the composite's high-temperature mechanical properties and possibly oxidation resistance.

The above discussion shows: CNCs have improved material toughness. High-quality reinforcing ingredients are crucial to the improvement of high-temperature properties. The CNCs' mechanical properties, especially hardness and strength at high temperatures, are significantly improved. Therefore, the development of ceramics with high strength and high toughness will follow the direction of developing a hybrid form of microcomposite and CNC. Next-generation ceramic materials are possibly wafer-reinforced CNCs, as well as crystal-whisker-reinforced CNCs and continuous-fiber-reinforced CNCs. [passage omitted]

4. Concluding Remarks

Ceramics and ceramic composites as structural materials at 1,204-1,371°C have been in application. Obstacles in mass utilization of the materials, especially in the automobile industry, include their high cost. The important research projects are how to ensure their reliability and reduce their cost. For applications in the temperature range 1,371-1,649°C, especially above 1,600°C, current CMCs still have a long way to go. Among the non-oxide/non-oxide CMCs, SiC/SiC, and SiC/Si_3N_4 are the focal materials for certain applications in the temperature range 1,371-1,600°C. For applications above 1,600°C in the atmosphere the most promising course seems to be developing oxide/oxide CMCs, i.e., oxide composites reinforced by oxide fibers. The key is the development of high-quality oxide fibers. The important course that leads to the development of ceramics with super-strength and super-toughness is to integrate the microscale and nanocomposite technologies to create new CMCs. Functionally gradient material (FGM) project will not only produce new materials but also help improve existing materials.

References

1. Ho, C. Y., El-Rahaiby, S. K., "Assessment of the Status of Ceramic Matrix Composites Technology in the United States and Abroad," CERAM. ENG. SCI. PROC., 1992; 13 (7-8): 3.

2. Schulz, Robert B., Ray, Johnson, D., "Transportation, Energy, and Ceramics," CERAM. ENG. SCI. PROC., 1991; 12 (7-8): 947.

3. Tallan, Norman M., "Air Force High-Temperature Materials Program," CERAM. ENG. SCI. PROC., 1991; 12 (7-8): 957.

4. Sheppard, Laurel M., "Enhancing Performance of Ceramic Composites," AM. CERAM. SOC. BULL., 1992; 71 (4): 617.

5. "Fabricating Functionally Gradient Materials," AM. CERAM. SOC. BULL., 1992; 71 (4): 624.

6. Nan Cewen, Zhang Lianmeng, Yuan Runzhang, "The Transfusion Phenomenon of Functionally Gradient Materials," GUISUANYAN XUEBAO [JOURNAL OF THE CHINESE CERAMICS SOCIETY] (in print).

7. Courtright, E. L., "Engineering Property Limitation of Structural Ceramics and Ceramic Composites Above 1,600°C," CERAM. ENG. SCI. PROC., 1991; 12 (9-10): 1725.

8. Le Huirong, Li Jianbao, Huang Yong, et al., "Effect of Glass Crystal Boundary Phase Property on the Mechanical Properties of Hot-Pressed Si_3N_4 Ceramic Composites Reinforced With SiC Whiskers for Strength and Toughness," Proceedings of National Conference on Structural Ceramics, Xianyang: Committee on Special Ceramics of the Chinese Ceramic Society, 1990, 10: 209 (in Chinese).

9. Han Licheng, Zhao Hong, He Yu, et al., "High-Temperature Oxidation Property and Fracture Property of TiB-30%(wt) ZrO_2 Ceramic Composite," ibid., 10: 67 (in Chinese).

10. Strife, J. R., Brennan, J. J., Prewo, K. M., "Status of Continuous Fiber-Reinforced Ceramic Matrix Composite Processing Technology," CERAM. ENG. SCI. PROC., 1990; 11 (7-8): 871.

11. Mah, T., Parthasarathy, T. A., "Processing and Mechanical Properties of $Al_2O_3/Y_3Al_5O_{12}$ (YAG) Eutectic Composite," CERAM. ENG. SCI. PROC., 1990; 11 (9-10): 1617.

12. Whalen, P. J., Narasimhan, D., Gasdaska, C. G., et al., "New High-Temperature Oxide Composite Reinforcement Material: Chrysberyl," CERAM. ENG. SCI. PROC., 1991; 12 (9-10): 1774.

13. Lipowitz, J., Rabe, J. A., Zonk, G. A., "Crystalline Silicon Fibers Derived From Organosilicon Polymers," In: Proc. of 2nd Ann. Hi Temp. Review, NASA Conference Pub. 10039, 1989: 71.

14. Guo Jingkun, Xu Yaopin, "Nanoscale Ceramics and Their Development," GUISUANYAN XUEBAO [JOURNAL OF THE CHINESE CERAMICS SOCIETY], 1992; (3) 286.

15. Niihara, H., "New Materials Design for Ceramic Structural Materials—Nanocomposite Materials" (English version), TECHNICAL JOURNAL OF THE CERAMIC SOCIETY OF JAPAN, 1991; 99 (10): 974.

16. Sasaki, M., Hirai, T., "Manufacture and Various Properties of Functionally Gradient Materials" (English version), ibid., p 1002.

17. Koizumi, M., "Recent Progress in Functionally Gradient Materials in Japan," CERAM. ENG. SCI. PROC., 1992; 13 (7-8): 333.

Study of Physico-Chemical Process in Laser Synthesis of Ultrafine SiC Powder

93FE0877A Beijing GUISUANYAN XUEBAO [JOURNAL OF THE CHINESE CERAMICS SOCIETY] in Chinese Vol 21 No 1, Feb 93; No 2, Apr 93

[Article by Sui Tongbo [7131 0681 3134], correspondent, and Wang Tingji [3769 1694 4694] of the Chinese Institute of Building Materials Science, Beijing 100024: "Study of Physico-Chemical Process in Laser Synthesis of Ultrafine SiC Powder"; MS received 24 May 91]

[Vol 21 No 1, Feb 93 pp 33-37]

[Text] **Part I. Experimental Laws, Powder Characteristics**

Abstract: A 50 W continuous-wave CO_2 laser was used as a heat source to induce the chemical reaction between SiH_4 and C_2H_4 for synthesizing ultrafine SiC powder. Experiments determine the parameters such as pressure p in the reaction chamber, atomic ratio C/Si in the gas, nozzle diameter 2r, and the relationship between laser power density and powder characteristics, as well as the physical and chemical properties of the synthesized product.

Key Words: laser, gas-phase chemical reaction, silicon carbide, ultrafine powder.

1. Introduction

Manufacturing powder by laser synthesis is one of the most competitive methods among powder production techniques. The synthesized powder meets all the ideal requirements as suggested by Bowen,[1] i.e., small particle size, narrow particle size distribution range, no agglomeration, spherical configuration, and high purity. The laser method of producing high-purity ultrafine powder was initiated by MIT.[2] Similar research has also been launched in Japan, France, and other countries.[3,4]

This experiment studies the rules and mechanism of synthesizing ultrafine SiC powder from the $SiH_4 + C_2H_4$ system with a 50 W continuous-wave (CW) CO_2 laser (wavelength 10.6 μm) as the heating source.

2. Experimental Work and Results

2.1 Experimental Process

The synthesis of ultrafine SiC powder is based on a gas-phase chemical reaction as follows:

$$SiH_4(g) + (1/2)C_2H_4(g) = SiC(s) + 3H_2(g).$$

Figure 1 shows the schematic diagram of the device arrangement for this experiment. Its main feature is that the flow directions of the mixed reacting gas are perpendicular to the laser beam. A mechanical vacuum pump evacuates the reaction chamber and the tubing system to an atmospheric pressure of about 1.33 Pa. The buffer gas Ar flows into the chamber window as well as into the nozzle through the respective mass flow controllers

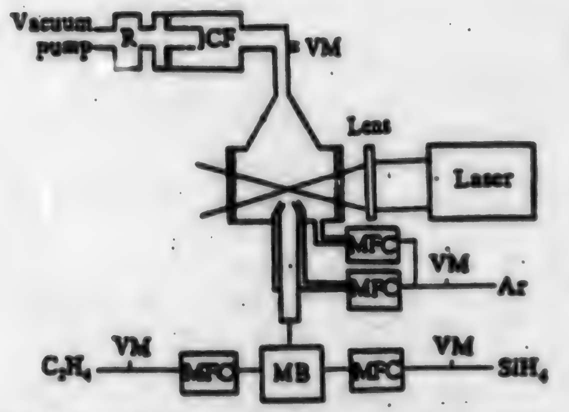

Figure 1. Schematic Drawing of Device for Laser Synthesis of Ultrafine SiC Powder

(MFC). Reaction gases, SiH_4 and C_2H_4, through their respective MFCs, flow into the mixing box (MB), and then the gas mixture enters the nozzle. The regulator (R) adjusts the pressure in the reaction chamber. The laser output power is 35-40 W. After the laser beam is focused with a KCl crystal lens, its power density reaches 860-1,000 W/cm^2. When the gas mixture of SiH_4 and C_2H_4 meets the focused laser beam, it quickly reaches the reaction temperature through its resonance with laser energy and the collision of atoms. The powder produced by the reaction is carried with Ar gas into the collector (CF). The reaction consumes about 10 percent of the laser energy and produces ultrafine SiC powder at a rate of 0.6 gram per hour.

2.2 Experiment on Reaction Conditions

2.2.1 Effect of the C/Si Atomic Ratio on the Gas Mixture

The inside diameter of the fixed nozzle is 2r = 1.0 mm. The pressure in the reaction chamber is p = 0.08 MPa. The fraction of free silicon (f-Si) in the product decreases with the increase of C/Si atomic ratio, as shown in Figure 2.

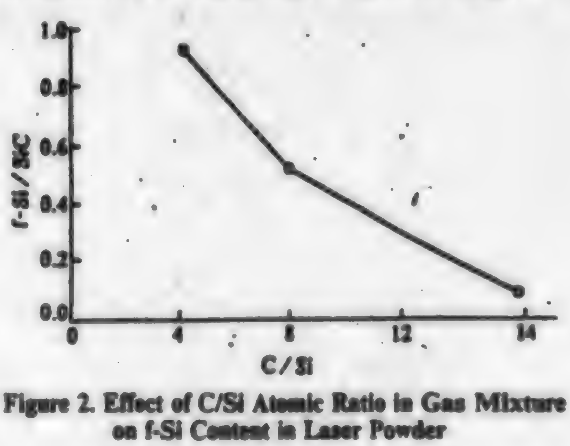

Figure 2. Effect of C/Si Atomic Ratio in Gas Mixture on f-Si Content in Laser Powder

2.2.2 Effect of Pressure p in Reaction Chamber

When all other conditions remain unchanged, the weight percent w of free silicon in the product decreases with reaction chamber pressure p, as shown in Figure 3.

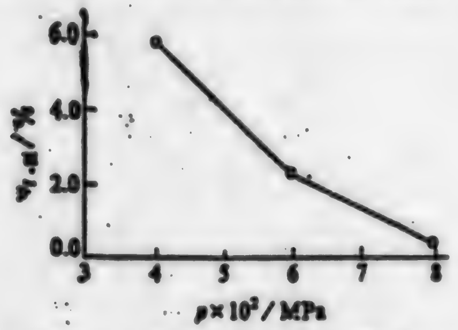

Figure 3. Effect of Cell Pressure p on f-Si Content in Laser Powder

2.2.3 Effect of the Nozzle's Inside Diameter 2r

2.2.3.1 2r = 0.50 mm: At a chamber pressure of $p \leq 0.10$ MPa, even when the flow ratio C_2H_4/SiH_4 is as high as 40/5, f-Si still exists in the product. The flow unit for both C_2H_4 and SiH_4 is mL/min.

2.2.3.2 2r = 1.0 mm: The f-Si can be practically eliminated under the conditions of $p \geq 0.08$ MPa and flow ratio $C_2H_4/SiH_4 \geq 40/4$; or $p \geq 0.10$ MPa and $C_2H_4/SiH_4 \geq 30/5$.

2.2.3.3 2r = 2.0 mm: The f-Si can be practically eliminated under the conditions of $p \geq 0.08$ MPa and $C_2H_4/SiH_4 \geq 20/10$; or $p \geq 0.04$ MPa and $C_2H_4/SiH_4 \geq 40/5$.

These results are consolidated in Figure 4, in which the shaded area represents the conditions under which f-Si will not exist in the product.

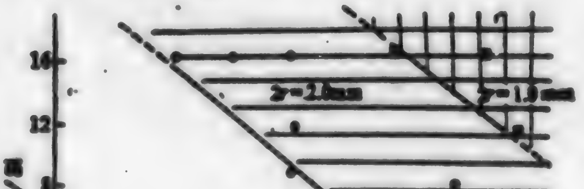

Figure 4. Experimental Conditions in Laser Synthesis of Ultrafine SiC Powder Without f-Si, Indicated by the Shaded Area

2.2.4 Effect of Focal Length of Lens

When the focal length of the lens is 50 mm or 100 mm, the reaction zone is small, resulting in low production rate, but the SiC powder tends to be crystalline because of the high laser power density and the high reaction temperature. When the focal length is 140 mm, the reaction zone is large, resulting in higher production, but the SiC powder is practically non-crystalline.

2.2.5 Effect of Ar

Argon flows into the system at two different locations: the nozzle and the chamber window. It serves two functions: as carrier gas and as protection gas. When the Ar flow rate into the nozzle is less than 0.40 L/min, the reaction zone is not stable and tends to disperse. When the Ar flow rate is 0.40 L/min or higher, the reaction is comparatively stable and tends to concentrate in a small zone. To obtain a stable flow into the chamber, the Ar flow rates in both paths are selected to be 0.40 L/min. In the experiment, Ar does not show other effects.

2.3 Powder Characteristics

The physical and chemical characteristics of the powder have been tested and analyzed with X-ray diffraction, electron diffraction, infrared absorption spectroscopy, transmission electron microscopy (TEM), emission spectroscopy, and chemical analysis. Table 1 shows the characteristics of the ultrafine SiC powder made under two typical sets of experimental conditions. Figure 5 [photographs not reproduced] shows the TEM photographs of the ultrafine SiC powder made under the two different conditions (a,b), respectively.

Table 1. Typical Experimental Conditions and Characteristics of SiC Powder Produced by Laser Synthesis Process

Laser power density/W-cm^{-2}		880-1000	
Lens focus/mm		140	
Nozzle inner diameter/mm	1.0		2.0
Cell pressure/MPa	0.08		0.08
Argon flow rate/L-min^{-1}	0.80		0.80
C_2H_4 flow rate/mL-min^{-1}	40		20
SiH_4 flow rate/mL-min^{-1}	5		10
Ultrafine SiC powder	(a)		(b)
Powder size/nm	10-18		20-35
Specific area/m^2-g^{-1}	98.5		76.5
Crystallinity	Some		No
SiC mass content/%		>96.0	
O_2 mass content/%		<2.34	
Metal content/10^{-5}		<10	

2.3.1 Physical Properties

Table 1 and Figure 5 show that the ultrafine SiC powder made by laser synthesis has high purity and is loosely agglomerated. Its grains are ultrafine (nanoscale), spherical, with narrow size distribution. The powder meets the ideal powder requirements. When the powder contains f-Si, it looks brownish; when it contains free carbon (f-C), it looks blackish. Grayish color indicates that the stoichiometric ratio of SiC is correct.

2.3.2 Chemical Properties

Chemical analysis shows that the synthesized product contains about 96.0 weight percent of SiC and very low metallic impurities. The main impurity in the powder is oxygen, which is adsorbed onto the highly active powder in the atmosphere. A small amount of oxygen enters the chamber along with Ar as well as with the reaction gases, and it forms oxide (combined oxygen) with the substances in the chamber. The oxygen content can be maintained at below 1.0 weight percent, if the powder is collected and stored in isolation from the atmosphere.

Figure 6 shows the infrared absorption spectrum of the powder. The strongest absorption peak indicates the Si-C bond.

2.3.3 Powder Crystalline State

The X-ray diffraction and electron diffraction analyses show that the product is mainly non-crystalline SiC with a small amount of β-SiC as shown in Figure 7.

3. Conclusions

(1) The ultra SiC powder made with a laser synthesis method meets the ideal powder specifications.

(2) The increase of the flow ratio C_2H_4/SiH_4, the pressure inside the reaction chamber, the nozzle inside diameter, and the laser power intensity reduce f-Si in the product. In other words, the product is closer to the SiC stoichiometric ratio.

(3) As shown in Figure 4, the conditions for the synthesizing of high-quality ultrafine SiC powder are not restricted to one point, but spread in a defined area.

(4) The SiC content in the product is above 96.0 weight percent.

References

1. Bowen, H. K., "Basic Research Needs on High-Temperature Ceramics for Energy Applications," MATER. SCI. ENG., 1980; 44(1): 1.

2. Cannon, W. R., Danforth, S. C., Flint, J. H., et al., "Sinterable Ceramic Powders From Laser-Driven Reactions," J. AM. CERAM. SOC., 1982; 65(7): 324.

3. Cauchetier, M., Croix, O., Luce, M., et al., "Laser Synthesis of Ultrafine Powder," CERAM. INTER., 1987; 13:13.

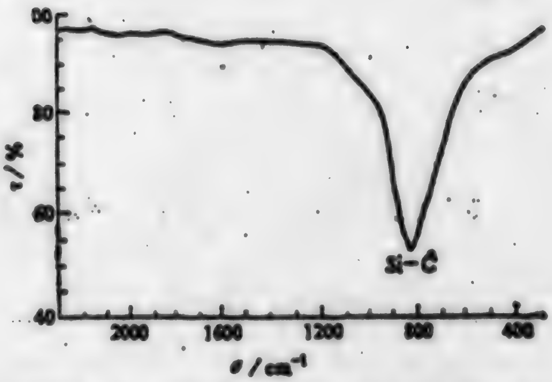

Figure 6. IR Absorption Spectrum of SiC Powder in KBr Pellets

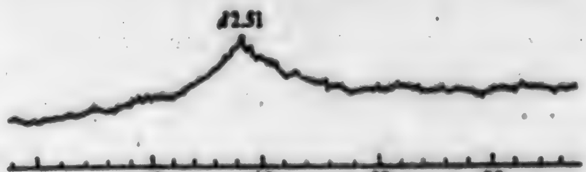

Figure 7. XRD Pattern of Ultrafine SiC Powder

4. Sawano, K., Haggerty, J. S., Bowen, H. K., "Formation of SiC Powders From Laser-Heated Vapor-Phase Relations," J. CERAM. SOC. JPN., 1987; 95: 64.

[Vol 21 No 2, Apr 93 pp 163-168]

[Excerpts] **Part II. Modeling, Analysis**

Abstract: Based on experimental results in Part I of this paper, and the law of conservation of energy, a simplified theoretical model is proposed. From the model, the relation between reaction temperature T and other technical parameters is derived as follows: $T = T_0 + (X/Y)[1 - \exp(-Y\tau/b)]$. Results calculated from this equation agree with the experimental results. The reaction feasibility and the production rate of ultrafine SiC powder are investigated according to the thermodynamic theories.

[Introduction]

The complexity of the entire chemical and physical process makes it difficult to describe the gas-phase chemical reaction induced by the laser. Haggerty et al.[1-3] did extensive work in this field. To further study the inherent rules of laser-produced power, this paper proposes a simplified theoretical model based on the experimental data. The model establishes a series of conclusions which agree with the experimental results. Based on thermodynamic theories and the simplified theoretical model, this paper analyzes and estimates the reaction feasibility and the powder production rate of the

laser process. The experimental parameters and powder characteristics are stated in Part I[4] of this paper.

1. Model and Analysis

1.1 Simplified Theoretical Model

Let us assume that after absorbing the laser energy, the material in the reaction zone maintains a thermal equilibrium state, then the total laser energy dE absorbed by the material is partially (dE') used for producing SiC; and the balance of the absorbed energy dE" is consumed by heat exchange with surrounding substances. The relation can be expressed in the following equation:

$$dE = dE' + dE'' \qquad (1)$$

After absorbing the laser energy, the reaction gases rapidly raise its temperature from the environmental temperature T_0 to the reaction temperature T. Through a series of calculations[5] from Equation (1), we can derive the relation between T and other parameters, namely, laser power output P, nozzle inside radius r, the length l of the laser heating zone, and the pressure p inside the reaction chamber. The derived equation is listed as follows:

$$T = T_0 + (X/Y)[1 - \exp(-Y\tau/b)] \qquad (2)$$

where:

X and Y are constants in the process parameters;

$X = [a_c\,(C/Si) + a_s\,P$;

$Y = c\,(Ar/Si)$;

τ is length of time the gases stay in the reaction zone and is given by $\tau = (\pi r^2/V)\,(p/p')\,l$;

a_c and a_s are the absorption constants at 10.6-μm wavelength for C_2H_4 and SiH_4, respectively;

C/Si and Ar/Si are the atomic ratios in the gas source, respectively;

p' is gas pressure in the tubing system;

V is total flow of C_2H_4 and SiH_4 in the gas source; and

b and c are ratio constants.

Equation (2) explains the test results of Part I of this paper quite satisfactorily under the assumption that the reaction product SiC depends on reaction temperature T, i.e., the higher the T, the more SiC product and the less free silicon (f-Si).

Figure 1 and Figure 2 display the theoretical curves plotted from Equation (2), where: $a_c = 0.1$, $a_s = 0.5$, $b = 0.1$, $c = 0.5$, $p' = 0.14$ MPa, $l = 0.20$ cm, and $P = 40$ W.

Figure 1 shows the relation between reaction temperature T and C/Si ratio in the gas source, inside nozzle diameter 2r, SiH_4 flow rate, and the chamber inside pressure p, when Ar/Si is fixed at 80.

Figure 1 also shows that reaction temperature T increases with increase in reaction chamber pressure, C/Si ratio in the gas source, and the inside diameter of the nozzle. This indicates that for the same reaction, a small-diameter nozzle requires higher gas pressure, and lower gas pressure will suffice for a larger-diameter nozzle. In other words, high reaction gas pressure for a large-diameter nozzle can effectively increase the reaction temperature and eliminate f-Si. The conclusion agrees with the experimental results in Part I of this paper.

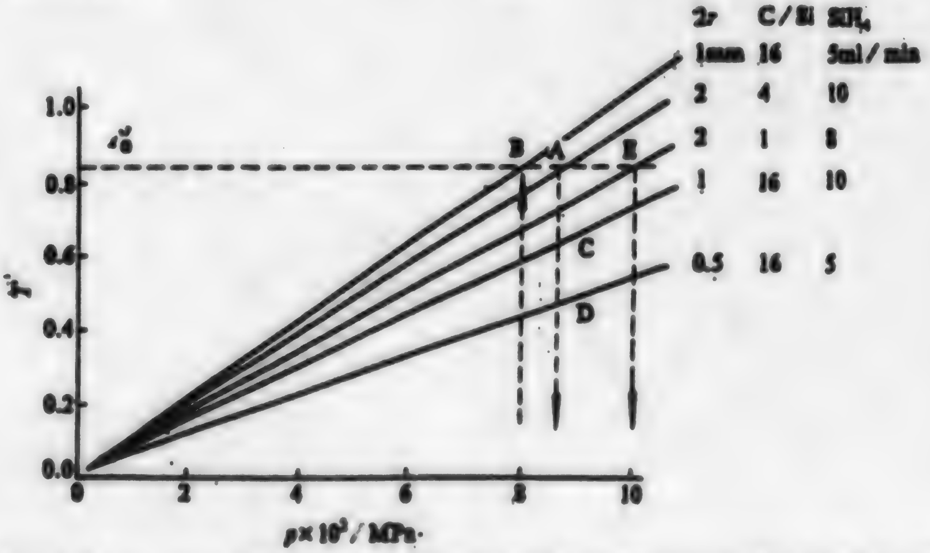

Figure 1. Theoretical Dependence of Reaction Temperature Upon Inner Diameter of the Nozzle 2r, C/Si Atomic Ratio in Gas Mixture, SiH_4 Flow Rate and Cell Pressure; T is a Normalized Temperature

Interestingly, the experiment has determined that f-Si can be eliminated under condition B ($2r = 1.0$ mm, $SiH_4 = 5$ ml/min, $p = 0.08$ MPa, and $C/Si = 16$). From Figure 1, reaction temperature T'_0 under this condition can be reached. Based on this finding, other conditions (A, C, D, and E) to achieve the same purpose can also be deduced as follows:

Condition A. $2r = 2.0$ mm, $SiH_4 = 10$ ml/min, $p = 0.085$ MPa, and $C/Si = 4$;

Condition C. $2r = 1.0$ mm, $SiH_4 = 10$ ml/min, $p > 0.1$ MPa, and $C/Si = 16$;

Condition D. $2r = 0.5$ mm, $SiH_4 = 5$ ml/min, $p > 0.1$ MPa, and $C/Si = 16$.

All the above agrees with the experimental results in Part I of this paper, and explains that the existence of f-Si is mainly caused by a temperature below the required reaction temperature.

It is worth mentioning that condition E ($2r = 2.0$ mm, $SiH_4 = 8$ ml/min, $p = 0.1$ MPa, and $C/Si = 1$) where $C/Si = 1$, is derived from condition B, which indicates that it is possible to use a low-power laser to produce ultrafine SiC powder conforming to the stoichiometric ratio. Experiments to prove the theory are in progress.

Figure 2 shows the relation between reaction temperature and atomic ratio Ar/Si in the gas source. Reaction temperatures rapidly decline with increase in Ar/Si ratio until Ar/Si reaches 60. From then on, changes of Ar/Si ratio are not apparent. The experiment in Part I used this Ar/Si value, which explains why the Ar content did not affect the experimental results. [Passage omitted]

2. Conclusions

(1) The fact that the simplified theoretical model and a series of deduced conclusions agree with the experiment as described in Part I indicates that to a certain degree they reflect the inherent rules of powder production by laser.

(2) The temperature equation (2) and production rate formulae (9-1 and 9-2) point out the direction of parameter adjustment as well as the target production rate.

(3) The conditions deduced from theoretical chemical reactions are considered the most scientific and economical working conditions. In theory, working under the conditions of theoretical reaction, it is possible to produce SiC with stoichiometric ratio through the use of low-power laser devices.

References

1. Haggerty, J. S., Cannon, W. R., "Laser-Induced Chemical Processes," New York: Plenum Press, 1981: 165.

2. Flint, J. H., Haggerty, J. S., "Models for Synthesis of Ceramic Powders by Vapor-Phase Reactions," In: Proc. of the 1st Inter. Conf. on Ceramic Powder Processing Science, Orlando, FL, November 1987 (to be published).

3. Flint, J. H., Marra, R. A., Haggerty, J. S., "Powder Temperature Size and Number Density in Laser-Driven Reactions," AEROSOL. SCI. TECH., 1986; 5:249.

4. Sui Tongbo, Wang Tingji, "Study of Physico-Chemical Process in Laser Synthesis of Ultrafine SiC Powder—I. Experimental Laws and Characteristics of the Powder," GUISUANYAN XUEBAO [JOURNAL OF THE CHINESE CERAMICS SOCIETY], 1993; 21(1) 33 [in Chinese].

5. Wang, T. J., Sui, T. B., Guan, Q. B., "A Study for Laser Synthesis of Ultrafine SiC Powders," In: Proc. CMRS Inter. '90, Beijing, June 1990 (to be published).

6. Xu Zhihong, Wang Leshan, "Inorganic Chemistry Data Base," Beijing: Science Publishing House, 1987:8 [in Chinese].

7. Cauchetier, M., Croix, O., Luce, M., "Laser Synthesis of SiC Powders From Silane and Hydrocarbon Mixtures," ADV. CERAM. MATER., 1988; 3:542.

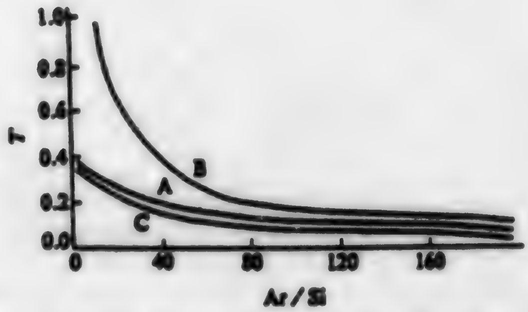

Figure 2. Theoretical Dependence of Reaction Temperature T Upon Ar/Si Atomic Ratio in Gas Mixture; T is a Normalized Temperature

Study of TiB_2-Ti(C,N) Ceramic Composites Prepared by Reactive Hot-Pressing

93FE0877B Beijing GUISUANYAN XUEBAO [JOURNAL OF THE CHINESE CERAMICS SOCIETY] in Chinese Vol 21 No 2, Apr 93 pp 182-187

[Article by Zhang Guojun [1728 0948 6511], correspondent, the Institute of Advanced Ceramic Technology, Chinese Academy of Building Materials Science, Beijing 100024: "Study of TiB_2-Ti(C,N) Multiphase Ceramics Prepared by Reactive Hot-Pressing"; MS received 21 Dec 91]

[Text] **Abstract**: Through chemical reaction design, TiB_2-Ti(C,N) ceramic composites (multi-phase ceramics) can be manufactured by the reactive hot-pressing method with Ti, TiH_2, BN, B_4C, C, B, etc., as raw materials. The method is simple and its manufacturing cost is low. SEM

shows that in the composites, ultrafine (about a few tens of nanometers) Ti(C,N) and TiB_2 crystals are distributed in the TiB_2 and $TiC_{0.5}N_{0.5}$ grains, respectively. This type of structure can possibly affect the material properties greatly. It deserves further research on the means to control this type of structure. Fracture surface analysis shows that transgranular fractures occur on the coarser TiB_2 crystals.

Key Words: Titanium diboride, titanium carbonitride, reactive hot pressing, microstructure, ceramic nanocomposite, reaction mechanism.

1. Introduction

The high melting point and hardness as well as the good chemical stability of the TiB_2 and Ti(C,N) compounds makes them good candidate materials for cutting tools and machine parts requiring good abrasive resistance. They also have good electrical conductivity which makes them candidates for electrodes.

As cutting-tool materials, TiB_2 has a higher hardness than Ti(C,N), while the nitrogen content in the latter can greatly decrease the friction coefficient during steel cutting. Both merits benefit the cutting process. Hence, ceramic composites made from TiB_2 and Ti(C,N) will have high hardness and low friction coefficient. Tadahiko Watanabe et al. conducted research on this material for many years with good results,[1-3] and believed the composite to be promising cutting-tool material. They used a two-step manufacturing process. First, TiB_2 and Ti(C,N) were synthesized separately, and then mixed together with other ingredients. The mixture was either hot-pressed[1,3] or sintered[2] to TiB_2-Ti(C,N) ceramic composite. The press-sintering method simplified the production technique and reduced the cost.[2] Currently, the bend strength of the composite made by the press-sintering method is 600 MPa, but the composite made by the hot-press method can reach 900 MPa. This investigation adopts a single-step process, i.e., reactive hot-pressing,[4] which mainly uses the following chemical reactions:

$$TiH_2 \longrightarrow Ti + H_2\uparrow$$

$$(1+\alpha)Ti + (1-x)BN + \frac{2\alpha+x-1}{4}B_4C + \frac{3x-2\alpha+1}{4}C \longrightarrow \alpha TiB_2 + TiC_xN_{1-x} \tag{1}$$

$$(1+\beta)Ti + (1-x)BN + xB_4C + (2\beta-3x-1)B \longrightarrow \beta TiB_2 + TiC_xN_{1-x} \tag{2}$$

where: $x = 0\text{-}1$, $\alpha = 0\text{-}2$, and $\beta \geq 2$. This process eliminates the synthesizing of raw materials, simplifies the manufacturing method, and thus greatly reduces the production cost. This paper presents the reaction mechanism during the course of reactive hot-pressing, the mechanism of the microstructure formation, and other related phenomena.

2. Experimental Work and Results

2.1 Sample Preparation

The experiment adopted reaction (1) with $x = 0.5$ and $\alpha = 1.25$. The starting materials were: TiH_2 (made by the Beijing Nonferrous Metals Research Institute), BN (made by Yingkou Fine Chemicals Plant), and B_4C (made by Mudanjiang Second Grinding Materials Plant). The quantity of each material was calculated according to reaction (1). To densify the hot-pressing product, 2 percent of Ni powder (made by the Beijing Iron and Steel Research Institute) was added. The purpose of using TiH_2 is that TiH_2 will decompose to reactive neo-titanium. Table 1 shows the properties of different starting powders. The raw materials were first mixed and then ground in an Al_2O_3 ball mill for 12 hours with alcohol as grinding medium. The ground mixture was dried and then hot-pressed in vacuum at 1,850°C and 25 MPa for 30 minutes.

Table 1. Properties of Various Powders

Powder	Chemical composition in mass percent	Particle size μm*
BN	BN (99.30), fB (0.13), fB_2O_3 (0.44), Na_2O (0.14), Fe_2O_3 (0.05), NiO (0.02)	Approx. 1
TiH_2	—	< 30
B_4C	—	5-8
Ni	—	< 0.1

*Obtained by SEM.

2.2 Property Measurements

2.2.1 Hardness: The specimens were strips made by electrospark cutting, followed by polishing. They were tested for Vickers hardness under a 20-Kg load. The result is the average of 10 readings.

2.2.2 Bending strength by a three-point test: The specimens were made by electrospark cutting. One side of each specimen was polished with a diamond grinder. The dimensions of a test specimen were: 2.7 mm x 4.7 mm x 35 mm. The span between the two supports was 20 mm. The loading speed was 0.5 mm/min. The result is the average of five tests.

2.2.3 Electrical resistance at room temperature: A four-point-probe method was used to measure electrical resistance at room temperature. The result is the average of five tests.

2.2.4 Phase analysis: The composite phases were analyzed by X-ray diffraction (XRD). Figure 1 shows the XRD spectrum. The boron content in the specimen was determined by chemical analysis, and its phase composition (weight percentage) was calculated.

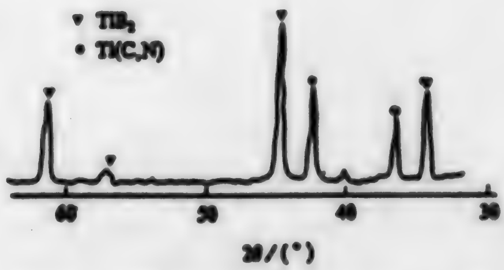

Figure 1. XRD Pattern of Ceramics Composite Produced by Reactive Hot Pressing

2.2.5 Microstructure analysis: A scanning electron microscope (SEM) with an electron acceleration voltage of 20 KV was used to study the microstructures of the polished surfaces and fracture surfaces.

Table 2 shows the test results.

Table 2. Properties of TiB_2-$TiC_{0.5}N_{0.5}$ Ceramic Composite

Relative density/%	Vickers hardness/ GPa	Bending strength/ MPa	Electrical resistance/ μΩ-cm	Mass composition of phase/%	
				TiB_2	$TiC_{0.5}N_{0.5}$
97.0	25	435 +/- 6.8	15.9	59.8	40.2

3. Analysis and Discussion

The XRD spectrum shows that there are only TiB_2 and Ti(C,N) phases in the ceramic composite. Chemical analysis also reveals that the composition of each phase is close to the composition derived from theoretical analysis. These facts indicate that the aforementioned chemical reactions are correct. We can assume that the adjustments of the values of α, β, and x in reactions (1) and (2) will change the mass ratio of TiB_2 and Ti(C,N) phases as well as the mass ratios of C and N in Ti(C,N). It is possible that the properties of TiB_2-Ti(C,N) ceramic composites can be adjusted within a wide range.

The binary phase diagrams of TiB_2-TiC and TiB_2-TiN show that at the experimental temperature the mutual solubility between TiB_2 and TiC or TiN is very limited and can be ignored. Further discussion will not consider the mutual solubility factors. Figure 2 [photographs not reproduced] shows the BSE morphology of the polished surface of the ceramic composite. In the photographs, TiB_2 appears to be dark gray; Ti(C,N), light gray; Ni, white; and gas holes, black. Figure 2 also shows the following features: very nonuniform distribution of TiB_2 and Ti(C,N) phases; gas holes; and a wide range of grain sizes. Some of the TiB_2 grains reach 10 μm, about the size of raw TiH_2 powder grains. Generally speaking, TiB_2 grains are much larger than Ti(C,N) grains. The additive, fusing-aid Ni, exists mainly in the interfaces among three grains.

In Figure 2b, the gas holes can be divided into two categories. One is called primary gas holes, which vary in sizes, some as large as 10 μm. Most of these gas holes are surrounded by grains. These holes are presumably generated by the arch-effect between particles during forming. Primary holes can be eliminated by adjusting powder properties and production conditions. Holes in the other category are called secondary gas holes; these are quite uniform in size, uniformly distributed, and exist in the triangular grain boundaries. The secondary gas holes are probably caused by two factors: First, inappropriate production technique that could not eliminate the residue gas holes during forming. Second—probably the main cause—these holes are produced by the differences of the solubilities of elements in liquid titanium during the course of reactive hot-pressing. The binary phase diagrams of Ti-B,[5] Ti-C, and T-N[6] show that at a hot-pressing temperature of 1,850°C, the maximum solubilities of B, C, and N in liquid titanium (Ti(l)) are 22, 9, and 2 atomic percent, respectively. When the compositions of B, C, and N exceed these solubility limits, Ti-B, TiC, and β-Ti will appear, respectively. However, when both B and C are in the solution, β-Ti may not exist in the Ti(l). Therefore, we can infer that TiN is formed along with the TiC formation according to the following reactions:

$$Ti(l) + C \rightarrow TiC(s) \quad (3)$$

$$\text{and } TiC + Ti(l) + C + N \rightarrow TiC_xN_{1-x}(s) \quad (4)$$

which means that the newly formed TiC acts as nuclei for the formation of TiC_xN_{1-x}. The formation of TiB_2 is due to the fact that the B quantity in liquid titanium exceeds the saturated concentration and produces the following reaction:

$$Ti(l) + 2B \rightarrow TiB_2(s) \qquad (5)$$

Due to the fact that the solubility of boron in Ti(l) is far greater than that of nitrogen, when both boron and nitrogen dissolve in Ti(l), the solution tends to reject nitrogen. Consequently, the rejected nitrogen is sealed in the specimen during hot-pressing and forms very minute holes. To eliminate these holes, the x value in TiC_xN_{1-x}, and the α and β values in reactions (1) and (2) should be adjusted so that the formation rates of TiB_2 and TiC_xN_{1-x} are compatible with the dissolving rates of B, C, and N in Ti(l). The aforementioned cause of nitrogen rejection is similar to the nitrogen rejection phenomenon caused by different solubilities of the elements in liquid Ni during the sintering of metallic ceramic TiN-Ni.[7]

Another remarkable phenomenon as shown in Figure 2a is the dispersion of segregated Ti(C,N) crystals in the TiB_2 grains. There is great variation in crystal sizes, about 10 nanometers. Similarly, the segregated nanoscale TiB_2 crystals also exist in the Ti(C,N) grains. The segregated TiB_2 crystals are even smaller than the segregated Ti(C,N) crystals. In another investigation, Williams et al.[8] discovered that the segregated TiC crystal flakes exist in TiB_2 and ZrB_2 single crystals, and the segregated TiB_2 crystals exist in TiC_x single crystals. The segregated crystals with sizes of a few nanometers were caused by the additives (such as B, etc.). They also thought that the segregated nanoscale crystals could modify the material properties, but they did not report further.

Figure 3 [photographs not reproduced] shows the SEM fractographs of TiB_2-$TiC_{0.5}N_{0.5}$ ceramic composite. It reveals that the crack propagates transgranularly when it encounters a large crystal grain. Figure 3d shows the morphology of a transgranular fracture, as well as the mode of crack propagation. When a crack extends to a large grain, it divides into a fork with one branch moving along the grain boundary while the other penetrates through the large grain. This observation shows that the TiB_2-$TiC_{0.5}N_{0.5}$ ceramic composite made by reactive hot-pressing method has higher grain boundary strength, which is possibly improved by the fusion-aid agent Ni. In other words, when the nanoscale TiB_2 and Ti(C,N) dispersion method is used to improve the properties of TiB_2-Ti(C,N) ceramic composite, measures should be taken to increase the grain boundary strength, so that the transgranular fracture will become the main failure mode.

4. Conclusions

(1) It is possible to make TiB_2-Ti(C,N) ceramic composite by the reactive hot-pressing process, which is simple and less expensive.

(2) When B, C, and N dissolve in Ti(l) and form a saturated solution, the formation of TiB_2-Ti(C,N) is postulated according to the following process:

$$Ti(l) + 2B \rightarrow TiB_2(s);$$

$$Ti(l) + C \rightarrow TiC(s);$$

$$\text{and } TiC(s) + Ti(l) + C + N \rightarrow Ti(C,N)(s).$$

(3) The nanoscale Ti(C,N) crystals disperse in the TiB_2 grains. At the same time, the nanoscale TiB_2 crystals also disperse in the Ti(C,N) grains. This phenomenon may affect the properties of the material. It requires further study.

(4) Cracks propagate transgranularly when they encounter large grains.

References

1. Ayameura, K., Watanabe, T., Yamamoto, H., "Hot-Press Sintering of Ti(CN)-TiB_2 System," JOURNAL OF THE CERAMICS SOCIETY OF JAPAN, 1985; 93(5): 252 [in Japanese].

2. Watanabe, T., "Oxide Addition Effects on Mechanical Properties of $Ti(C_{0.5}N_{0.5}$-30 wt% TiB_2 Carbide System Sintering," ACADEMIC JOURNAL OF THE CERAMIC SOCIETY OF JAPAN, 1991; 99(2): 146 [in Japanese].

3. Watanabe, T., Yamamoto, H., Shobu, K., et al., "Factors Affecting the Porosity and Bending Strength of Ti(CN)-TiB_2 Materials," J. AMER. CERAM. SOC., 1988; 11(4): C-202.

4. Zhang Guojun, "Manufacturing Titanium Nitride-Titanium Boride Ceramics by Reactive Hot-Pressing Method," Co4B35/58, Chinese patent, 1056859A, 1991-12-11.

5. Samsonov, G. V., "Handbook of Infusible Compounds" [in Russian], translated by the Editorial Office, Institute of Science and Technology Information and Product Standards Research, Ministry of Metallurgical Industry, Beijing: China Industries Publ. House, 1965:353.

6. Toth, L. E., "Transition Metal Carbides and Nitrides," New York and London: Academic Press, 1971: 72, 88.

7. Fukuhara, K., Mitani, H., "Correlation System and Denitrification of TiN-Ni Mixture Pressurized Powder," JOURNAL OF THE JAPAN INSTITUTE OF METALS, 1979; 43(3): 169 [in Japanese].

8. Mochel, P., Allison, C., Williams, W. S., "Study of Titanium Carbide Precipitates in Titanium Diboride by Electron Energy Loss Spectroscopy," J. AMER. CERAM. SOC., 1981; 64 (4): 185.

Further Reports on Nanomaterials

Effect of Cu, Nb on Fe-Si-B Amorphous Alloy-Based Nanocrystals

94FE0062A Beijing KEXUE TONGBAO [CHINESE SCIENCE BULLETIN] in Chinese Vol 38 No 13, 1-15 Jul 93 pp 1244-1246

[Article by Yang Huisheng [2799 2585 3932], Zhang Shoulu [1728 1108 4389], Ma Ruzhang [7456 1172 3864], and Lin Qin [2651 0530] of the Department of Material Physics, Beijing Science and Technology University, Beijing 100083; Zhang Jiaji [1728 1367 7535] and Tu Guochao [3205 0948 6389] of the Institute of Metallurgy, Capital Steel Works, Beijing 100085: "Study of Cu, Nb Effect on Formation of Nanocrystals From Fe-Si-B Amorphous Alloys," funded by NSFC; MS received 22 Jun 92, revised 10 Nov 92]

[Text] A few multi-component alloy-based nanocrystals have been made by the amorphous alloy crystallization method. The typical composition is Fe-M'-M"-Si-B,[1] where M' represents Cu; M", the element Nb, Mo, V, Hf, or Ta. M' and M" are nanocrystal-forming elements.[2] Due to their superior comprehensive soft magnetic characteristics, these types of nanocrystal alloys have become new-generation materials for soft magnets. At present great achievements have been made in manufacturing technology and the magnetic study of nanocrystal alloys. However, the mechanism of the forming elements is still not very clear. In order to uncover the functions of the nanocrystal-forming elements, this paper employs the DTA (or DSC) [differential thermal analysis (or differential scanning calorimetry)] method to study the effects of the additive elements Cu and Nb on the activation energy of crystallization when crystallizing the Fe-Ni-B amorphous alloys.

1. Experimental Method

In solid state reaction, we have the following equation:

$$\frac{d\alpha}{dt} = \frac{A}{\Phi} e^{\frac{-E}{RT}} f(\alpha),$$

where α is reaction rate; T, temperature; A, frequency factor; Φ, temperature increasing rate; f(α), reaction function; and E, activation energy of crystallization.

By integration (Doyle-[phonetic] method),[3] we obtain the following relation:

$$\lg \Phi = \lg \frac{AE}{RF(\alpha)} - 2.315 - 0.4567 E/RT.$$

When α is a constant, F(α) is also a constant. When lg Φ vs 1/T is plotted, the slope is (-0.4567 E/R). From the slope, we can obtain the activation crystallization energy E of the different crystallizing fractions.

The amorphous alloys for this experiment were in tape form and made by the single-roll chilling method. The specimens' compositions were $Fe_{73.5}Cu_1Nb_3Si_{13.5}B_9$, $Fe_{76.5}Cu_1Si_{13.5}B_9$, and $Fe_{77.5}Si_{13.5}B_9$(at%). The dimensions of each specimen were 10 mm x 18 μm. The analysis of $Fe_{73.5}Cu_1Nb_3Si_{13.5}B_9$ was conducted with DTA due to its high crystallization temperature. The analyses of the other two alloys were conducted with DSC.

2. Results and Discussions

Every DTA or DSC curve of the Fe-Si-B alloys displays two exothermic peaks. The first exothermic peak corresponds to the α-Fe solid solution segregation. The second peak is related to the formation of the boride. This experiment studies only the process of the α-Fe solid solution segregation. Specimens are made from each of the three alloys. The individual specimen is annealed at each of a series of temperatures for 30 min. The room-temperature X-ray diffraction data of these treated specimens are analyzed. The ratio of the α-Fe (200) peak intensity to the total intensity of the amorphous peak and the (200) peak is used to indicate crystallized fraction. The average crystal size of the α-Fe solid solution is measured with the Scherrer method. The results show that after crystallization, the average dimensions of the segregated α-Fe solid solutions of Fe-Cu-Si-B, and Fe-Si-B are both greater than 1 μm. Yet, when the alloys are annealed to the temperature range of 480-630°C, the α-Fe solid solution crystal dimensions of the crystallized Fe-Cu-Nb-Si-B alloy stay constant, at about 100 angstroms, as shown in Figure 1. When the alloy is annealed above 630°C, boride is formed, and the α-Fe crystals grow conspicuously.

During the crystallization of these three alloys, the crystallizing activation energy changes with the crystallized fraction as shown in Figure 2. For the Fe-Si-B alloys, the crystallizing activation energies practically maintain constant, at about 295 kJ/mol. For the Fe-Cu-Si-B alloys, the crystallizing activation energies monotonically increase with an increase in the crystallized fraction. For the Fe-Cu-Nb-Si-B alloys, the crystallizing activation energies are low in the early crystallization stage, but rapidly increase to 420 kJ/mol, then increase gradually, and again increase at a greater speed in the last stage.

The aforementioned experiments show that the addition of Cu markedly reduces the crystallizing activation energy, and the increase of Nb markedly raises the crystallizing activation energy. Past experiments[4] indicate that the most important factor affecting the stability of the amorphous alloy is the migration potential energy Δμ, because it represses the coordinated rearrangement. The experiments also show that an increase in Δμ will

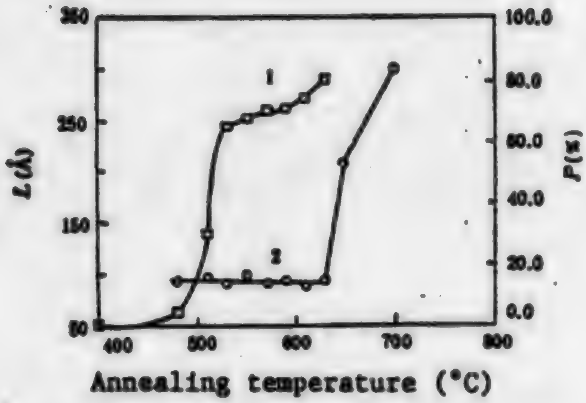

Figure 1. Crystallization of Amorphous $Fe_{73.5}Cu_1Nb_3Si_{13.5}B_9$ Alloy, Temperature vs Crystallized Fraction and Average Grain Size (L) of α-Fe Solid Solution

1: Crystallized fraction, 2: Grain size

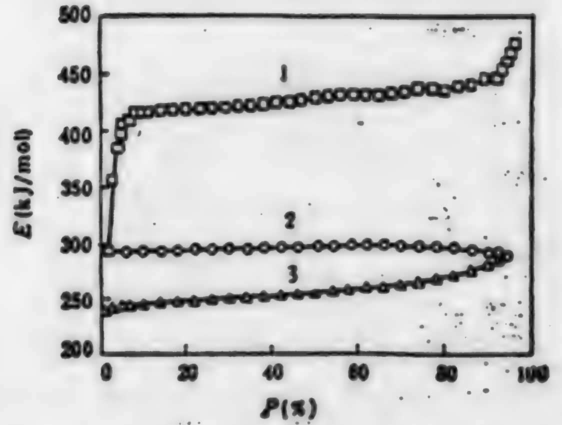

Figure 2. Activation Energy vs Crystallized Fraction of Different Alloys

1: $Fe_{73.5}Cu_1Nb_3Si_{13.5}B_9$, 2: $Fe_{77.5}Si_{13.5}B_9$, 3: $Fe_{76.5}Cu_1Si_{13.5}B_9$

increase the stability of the amorphous alloy. Δμ is related to the cohesive energy which controls the tendencies of repulsion or attraction among atoms. Chen Heshou points out that interactions among atoms increase as the differences of electròn negativities of the constituents amplify. The quasi-chemical approximation method is used to calculate the interaction parameters and the bonding energies among atoms in the amorphous alloys. Assuming that ε_{AA}, ε_{BB}, and ε_{AB} are the bonding energies of atomic pairs A-A, B-B and A-B, respectively; ω_{AB} is the interaction parameter of the A-B atomic pair, X_A and X_B are the electron negativities of A and B atoms, respectively, then

$$N_0\omega_{AB} = 96.5(X_A - X_B)^2,$$

$$N_0\varepsilon_{AB} = N_0\omega_{AB} + \frac{N_0}{2}(\omega_{AA} + \omega_{AB}),$$

as shown in Table 1. The Nb atoms have higher interaction parameters and bonding energies with the other atoms, significantly higher with the B atoms. Table 1 shows that there is a selective interaction between the Nb and B atoms. The interaction parameters and bonding energies between the Cu atoms and the other atoms are comparatively smaller and hence the interactions are weaker. Therefore, the addition of Cu in the Fe-Si-B alloy will weaken the interactions with the surrounding atoms, lower Δμ, decrease the stability, and consequently make the crystallization easy. To the contrary, the addition of Nb will strengthen the interactions with the surrounding atoms, increase Δμ, promote the stability, and consequently make the crystallization difficult. In the Fe-Cu-Nb-Si-B alloy, a dual effect is caused by Cu and Nb. In the early stage, crystallizations occur in the regions with higher Cu content and small activation energy. As the crystallization reaction proceeds, the Cu content drops. In combination with the Nb effect, the crystallized activation energy gradually increases, as shown in Figure 2.

Table 1. Interaction Parameters and Bonding Energy Among Atoms in Alloys

Atom	Negativity	Interaction parameter (kJ/mol)					Bonding energy (kJ/mol)				
		Fe	Si	B	Cu	Nb	Fe	Si	B	Cu	Nb
Fe	1.83	-					203.00				
Si	1.90	0.478	-				190.47	177.00			
B	2.04	4.256	1.891	-			232.26	216.89	253.00		
Cu	1.90	0.473	0.000	1.891	-		187.97	174.50	214.39	172.00	
Nb	1.60	5.105	8.685	16.682	8.685	-	349.10	339.70	387.80	337.10	485.00

As the Nb and B atoms are difficult to dissolve in α-Fe, they will be repelled to unrestricted phase boundaries and form separate conglomerates. The selective interaction between the Nb and B atoms will proceed along the grain boundaries and form into stable atom clusters which will inhibit the migration of the grain boundaries. The reaction will make the growth of the α-Fe solid solution crystals difficult. Eventually, the nanocrystalline structure is formed in the Fe-Cu-Nb-Si-B alloys.

3. Conclusions

The addition of Cu greatly reduces the activation energy of the Fe base amorphous alloy, but Nb effectively increases the activation energy. Furthermore, the Cu atoms increase the crystallizing nuclei, and the Nb atoms react with the B atoms thus creating atomic clusters which will prevent the growth of the α-Fe solid solution crystals. As a result, this combined effect achieves the formation of a nanocrystal structure in the Fe-Cu-Nb-Si-B alloys.

References

1. Yoshizawa, Y., Yamuchi, K., IEEE TRANSACTIONS ON MAGNETICS, 1989, 25(5): 3324-3326.

2. Yoshizawa, Y., Yamuchi, K., MATERIALS TRANSACTIONS, JIM, 1990, 31(4): 307-314.

3. Li Yuzeng, "Thermoanalysis," Qinghua University Press, 1987, 82 [in Chinese].

4. Yang Yinshan, Wan Yihe, "Amorphous Alloys," Metallurgical Industry Press, Beijing, 1989, 6-9.

Nanoscale Solids Via Sputtering/Condensation/In-Situ Pressurization

94FE0062B Beijing KEXUE TONGBAO [CHINESE SCIENCE BULLETIN] in Chinese Vol 38 No 13, 1-15 Jul 93 p 1247

[Letter by Zhu Yong [2612 0516] and Qin Yong [4440 0516] of the Institute of Solid State Physics, Chinese Academy of Sciences, Hefei 230031: "Nanoscale Solid Mo and Mo_2N Made by Direct-Current Magnetron Sputtering/Chilled Condensation/In-Situ Pressurization Method," funded by NSFC; MS receipt date not given]

[Text] Nanoscale solid materials are bulk solid materials constituted with ultrafine particles having quantum surface effects and volume effects. They are a new and currently emerging active field in materials development. This paper presents some of the experimental results of preparing nanoscale solid molybdenum and Mo_2N with the magnetron sputtering/chilled condensation/in-situ pressurization method.

The nanoscale solid materials are manufactured with a locally made IAC-1 apparatus, which performs the glow-discharge/chilled condensation/in-situ pressurization process including the following functions: direct-current (d.c.)/radio-frequency magnetron (reaction) sputtering; resistance-heated glow plasma reaction; and resistance-heated bipolar sputtering/chilled condensation/in-situ pressurization. The equipment has the following advantages: no crucible contamination and capability of manufacturing complicated materials such as conductors, semiconductors, insulators, and other materials made by gas (oxygen, nitrogen, etc.) reactions. The d.c. magnetron sputtering/chilled condensation/in-situ pressurization process and the pure Mo target (3N) are used to make the nanoscale Mo and Mo_2N solids. First, the vacuum chamber is evacuated to a pressure of 4×10^{-4} Pa, and then back-filled with circulation gas. To make the nanoscale Mo solid, the back-fill gas is argon at 0.5 Pa and the d.c. sputtering parameters are 0.4 kV and 2 A. The cold trap on top of the vacuum chamber is cooled with liquid nitrogen. When the cold trap collects enough ultrafine particles, the sputtering is stopped and the chamber is evacuated to 4×10^{-4} Pa again. The ultrafine particles are transferred to the in-situ pressurization equipment, and pressed into shape under 1.5 GPa pressure at room temperature. The specimen diameter is 8 mm. The circular specimen made from all the particles produced after a 20-minute sputtering weighs 137 mg, and its specific gravity measured by weighing method is 7 g/cm^3, about 69 percent that of solid Mo. The average particle size is 8 nm, and quite uniform. The particle's crystal structure is body-centered cubic. When the chamber is back-filled with 0.2 Pa high-purity argon and followed with 0.5 Pa high-purity nitrogen, the face-centered cubic Mo_2N particles are formed. The average particle size is also 8 nm. The results of microhardness tests are: for the nanoscale Mo solid, $H_v = 824$ kg/mm^2, about three times that of metallic Mo; for the nanoscale Mo_2N, $H_v = 1850$ kg/mm^2. The test results show that the microhardness of the non-sintered nanoscale Mo solid with an average particle size of 8 nm still agrees with the trend of the Hall-Petch relation.

The nanoscale solid particles made by this method have comparatively uniform particle size, because the condition of sputtering or evaporation is quite constant at the target surface. When nitrogen is introduced, the target surface is activated by the plasma, the surfaces of the sputtered materials are also activated, and the nitrogen molecules are ionized. Therefore, when the conditions are right, nitrides are easily formed. These are the main reasons why it is possible to produce the nanoscale Mo and Mo_2N solids with comparatively uniform particle sizes.

Preparation of, Quantum Size Effects in CdS-Glass 0-3-nm Composites

94FE0097A Beijing KEXUE TONGBAO [CHINESE SCIENCE BULLETIN] in Chinese Vol 38 No 17, 1-15 Sep 93 pp 1622-1625

[Article by Lu Shengguo [7627 5110 0948], Zhang Liangyin [1728 5328 3853], and Yao Xi [1201 3588] of the Electronic Materials Research Laboratory at Xian Jiaotong University, Xian 710049, and Xie Qingyun [6200 7230 0061] of the Xian Electro-Ceramics

Research Institute, Xian 710077: "Preparation of, Quantum Size Effects in CdS-Glass 0-3-nm Composites," supported by grant from the State "863" High-Tech New Materials Fund; MS received 27 Sep 92, revised 28 Apr 93]

[Text] Key words: Sol-gel technology, In-situ growth, Nanocomposites, Quantum size effects.

1. Introduction

With the development of high and new technologies, optoelectronics has seen a pressing demand for nonlinear optical materials. Since the Japanese physicist Ryogo Kubo first reported the "Kubo effect"[1] in nanoscale metal particles, nanoscale materials research has become very active. Its scope has expanded to include metal oxides, polarized compounds, and semiconductors.[2-4]

Nanocomposites provide an easier method to study low-dimensional quantum-well materials (quantum dots, quantum wires, etc.). The 0-3-nm composite is a composite with a 3-dimensional matrix in which the 0-dimensional quantum dots are dispersed. The 3-dimensional matrix is made of glass, polymer, or inorganic crystals. Recent theoretical study reveals that when the crystal size is less than 10 nm, the 3-stage nonlinear polarization rate and response speed will increase.[5]

In this paper, we use the sol-gel technique and in-situ growth technology to make the 0-3-nm glass composite dispersed with CdS whose crystal size is 3 to 6 nm. Its absorption edge and fluorescence peak have the blue shift characteristic.

2. Experiment

The $CdO-SiO_2$ gel glass is made by a two-step hydrolysis technique.[6] The CdO contents in $CdO-SiO_2$ are 1, 2, 5, and 10 wt%, respectively. The purity of all the chemicals is of analytical grade.

The experimental procedures are as follows:

(1) Drip silicate acetate (TEOS) into a solution (pH = 1.0-2.0) of water, ethanol and hydrochloric, then stir the solution for 1 hour;

(2) Dissolve cadmium acetate in methanol;

(3) Pour solution (2) into solution (1), stir for 30 min, then pour the mixed solution into the basic solution of ethanol and water (pH = 10.5-11.5);

(4) Stir the solution for 5 to 30 min, pour the solution in a glassware (after 1 to 2 days, the solution forms a wet gel), then leave the gelled solution to dry at room temperature for 5 to 15 days;

(5) Heat treat the dried gel at 500-700°C for a few hours so that a porous gel glass is formed;

(6) Set the porous gel glass to react with H_2S in vacuum to form the yellowish CdS microcrystals, which is the final specimen.

The specimen density is 2.0 gm/cm^3 by the Archimedes method. Its refractivity is 1.3-1.4 measured with an ellipsometer.

The x-ray diffraction spectrograph is conducted with a Lixue D/max-RB; the ultraviolet absorption is conducted with a Shimadzu UV-240, and the fluorescent spectrograph is measured with an LS-50 made by PE Company.

3. Results and Discussion

3.1 XRD Analysis

The x-ray diffraction analysis is conducted with CuKα radiation. The diffraction angle range is from 15° to 60° with an increment of 0.04°; scanning speed, 10°/min; voltage, 50 kV; and current, 200 mA. Figure 1 shows the x-ray diffraction curves. Based on the JCPDS card, the CdS microcrystal is determined to be of the wurtzite structure. Figure 2 shows a computer-adjusted curve with clearer peak separation. The crystal grain size is determined with the Scherrer formula[7]

$$D_{hkl} = k\,(\lambda/\beta \cos\theta) \qquad (1)$$

where D_{hkl} is the grain size perpendicular to (hkl); λ, x-ray wavelength; β, the factor denoting the peak widening caused by the fineness of the crystal; θ, the Bragg angle of the peak; k, a constant related to β (when β is the integrated width, then k = 1; if β is the mid-peak width, k = 0.9). Table 1 shows the diffraction results after the deduction of instrument radiation width.

Table 1. Peak Parameters and Crystal Size

Peak position (2θ)	Peak intensity	Full width at half maximum	Plane index	Crystal linear dimension (nm)
24.695	424	2.9859	100	3.0
26.561	551	2.3533	002	3.5
28.304	436	2.2884	101	3.6
43.935	604	2.4115	110	3.8
47.973	322	3.9670	103	2.2
50.504	79	1.6483	200	5.3
51.706	371	1.7319	112	5.1
52.633	256	1.9415	201	4.0
54.410	47	1.6767	004	5.3

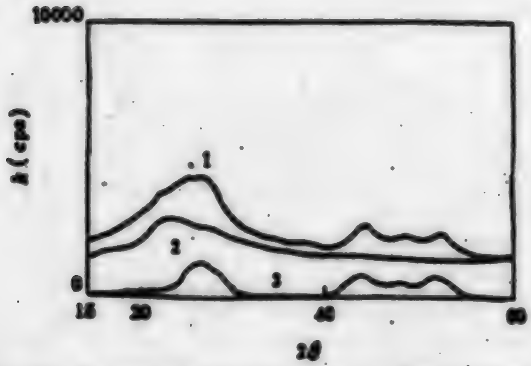

Figure 1. XRD Spectrograph of CdS Microcrystals

1. $CdS-SiO_2$; 2. $CdO-SiO_2$; 3. CdS

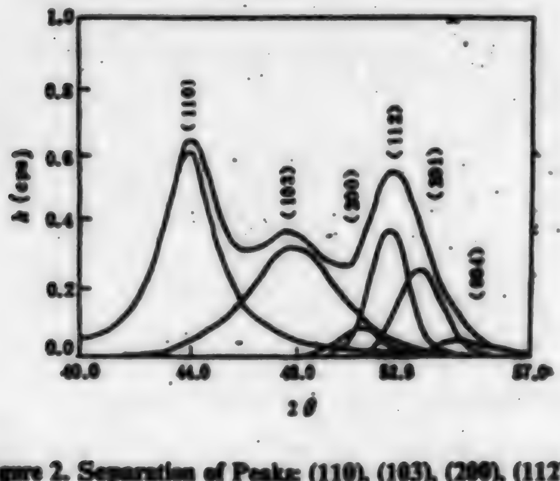

Figure 2. Separation of Peaks: (110), (103), (200), (112), (201), and (004)

3.2 Absorption Spectrograph

The absorption spectrograph is measured within the range of 190 nm to 900 nm. The shift of the absorption edge is observed among $CdS-SiO_2$ specimens of different reaction times. Figure 3 shows the absorption spectrograph.

3.3 Fluorescent Spectrograph

Figure 4 shows the fluorescent spectrograph of the $CdS-SiO_2$ composites with different reaction times. The excitation wavelength is 420 nm; filter cut-off wavelength, 430 nm. As the reaction time is reduced, the peaks in the neighborhood of 480 nm and the peaks of 500-700 nm shift in the direction of shorter wavelength. This is the blue-shift characteristic. However, the shift is relatively smaller compared to the shift of the absorption edge.

3.4 Quantum Size Effects

When the corresponding energy of the absorption edge is considered as the shift (transition) energy between

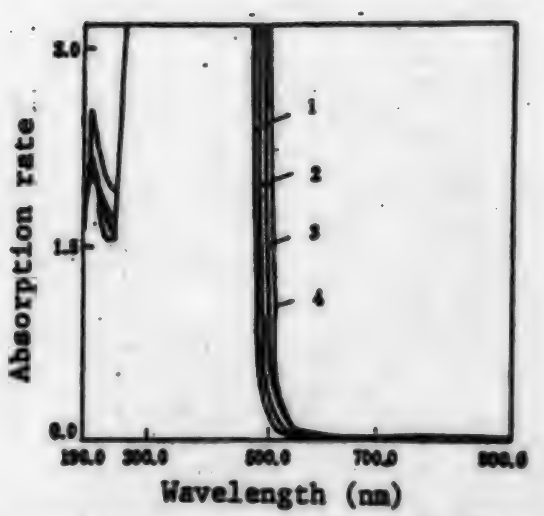

Figure 3. Absorption Spectrograph of $CdS-SiO_2$ vs Reaction With H_2S

1: 0.5 hr; 2: 1 hr; 3: 10 hr; 4: 48 hr

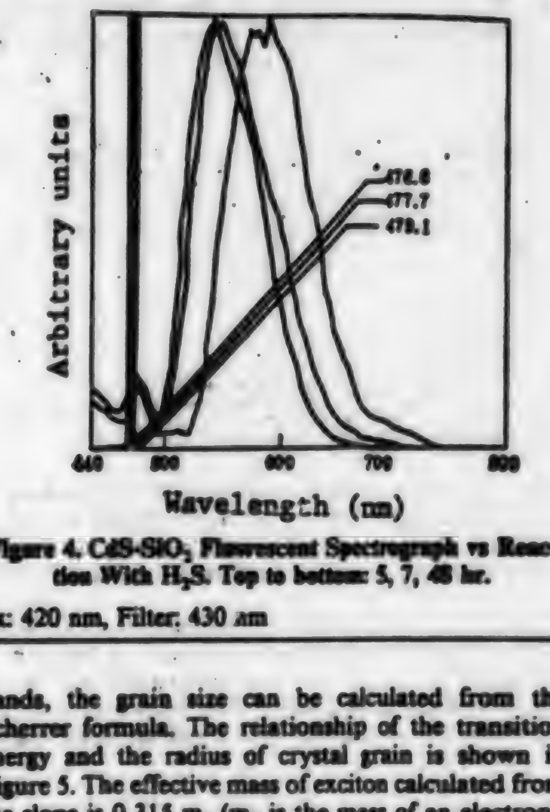

Figure 4. $CdS-SiO_2$ Fluorescent Spectrograph vs Reaction With H_2S. Top to bottom: 5, 7, 48 hr.

Ex: 420 nm, Filter: 430 nm

bands, the grain size can be calculated from the Scherrer formula. The relationship of the transition energy and the radius of crystal grain is shown in Figure 5. The effective mass of exciton calculated from the slope is 0.315 m_0 (m_0 is the mass of an electron). This value is smaller than the horizontally moving exciton mass $M = 0.99\ m_0$. When we consider the Bohr radius of exciton, $a_B = 2.62$ nm, in the CdS matrix, then it is reasonable that the combined reduced mass of electron and hole μ ($1/\mu = 1/m_e + 1/m_h$) can be used as the exciton mass. The reduced mass of exciton in the CdS matrix is about 0.154 m_0.

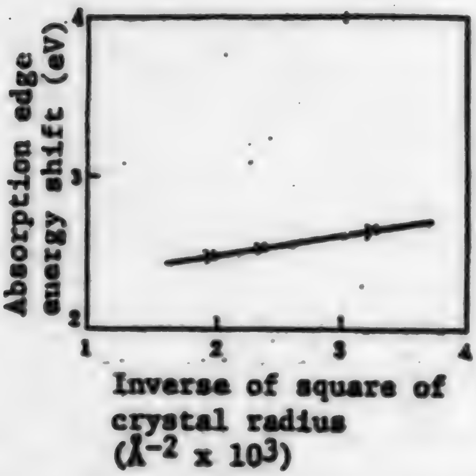

Figure 5. Energy Shift vs Inverse of Square of Crystal Radius

Considering the mutual coulomb effect between the electrons and the holes in the three-dimensional quantum wells, as well as the electron polarization, Brus arrives at the following equation:[8]

$$E = \frac{\hbar^2\pi^2}{2R^2}\left(\frac{1}{m_e} + \frac{1}{m_h}\right) - \frac{1.8e^2}{R} + \frac{e^2}{R}\sum_{n=1}^{\infty} \alpha_n \left(\frac{S}{R}\right)^{2n}, \qquad (2)$$

in which

$$\alpha_n = \frac{(\varepsilon - 1)(n + 1)}{\varepsilon_1(\varepsilon n + n + 1)}, \qquad (3)$$

where $\varepsilon = \varepsilon_2/\varepsilon_1$; ε_1 is the matrix dielectric constant; ε_2, the CdS crystal dielectric constant; S, the site coordinate; m_e, the effective mass of an electron; m_h, the effective mass of a hole; and h[bar] is Planck's constant ($h/2\pi$).

The energy values (Table 2) calculated from Eq. (2) are higher than the experimental values. It is possible that some of the excitons move horizontally and possess kinetic energy E = h[bar]$^2\pi^2$/2MR^2 ($M = m_e + m_h$). In other words, some of the crystal radii are larger than the Bohr radius a_B. The exciton effective mass from this experiment is different from that obtained by Potter and Simmons.[9] Their exciton mass in the CdS glass composite made by the melting method is $M_{mass} = 0.92\ m_0$, which is close to the horizontal transition mass. In our opinion, the difference between their result and ours is possibly due to the difference of CdS grain sizes in the two experiments.

Table 2. Electron Hole Energy (units = eV) From Eq. (2)

Energy	Grain size		
	2.25 nm	2.05 nm	1.75 nm
Kinetic energy[a)]	0.480	0.578	0.793
Coulomb[b)]	-0.200	-0.220	-0.257
Polarization energy[c)]	0.067	0.073	0.086
Total energy	0.347	0.431	0.622
Absorption edge transition energy[d)]	0.100	0.151	0.254

a) First term of Eq. (2); b) second term of Eq. (2); c) third term of Eq. (2); d) the difference between the maximum corresponding absorption energy and the matrix material bandwidth energy.

Acknowledgment: The authors are grateful for the valuable discussions with Dr. R. B. Findlay.

References

1. Kubo, R., J. PHYS. SOC. JAPAN, 1962, 17: 976-986.

2. Gleiter, H., MATER. SCI. ENG., 1982, 52: 91-131.

3. Yumoto, Hiroiuki, and Asahara, Yoshiuki, SOLID STATE PHYSICS, 1989, 24(11): 111-116 [in Japanese].

4. Ekimov, A. L., et al., SOLID STATE COMMUN., 1985, 56(11): 921-924.

5. Hanamura, E., PHYS. REV., 1988, B38(2): 1228-1234.

6. Nogami, M., et al., J. NON-CRYST. SOLIDS, 1990, 122(1): 101-106.

7. Analysis Center (ed.), XRD Handbook, Rigaku Electromachinery Co., Ltd., 1985, 71.

8. Brus, L. E., J. CHEM. PHYS., 1984, 80(9): 4403-4409.

9. Potter, B. G., Simmons, J. H., PHYS. REV., 1988, B37(18): 10838-10845.

Ultrathin PMMA LB Films for X-Ray High-Resolution Lithography

94FE0068B Beijing GAO JISHU TONGXUN [HIGH TECHNOLOGY LETTERS] in Chinese Vol 3 No 6, Jun 93 pp 18-21

[Article by Gu Ning [7357 1337], Lu Wu [7627 2976], Lu Zuhong [7120 4371 1347], and Wei Yu [7279 6877] of Wu Chienshiung Lab, Southeast University, Nanjing, 210018; Shen Haoying [3088 3185 3467] of Nanjing Institute of Electron Devices, Nanjing, 210016; Tian Chaoyang [3944 6389 2799], Kan Ya [7074 1246], and Liu Zewen [0491 3419 2429] of the National Synchrotron Radiation Laboratory, University of Science and Technology of China, Hefei, 230026: "Ultrathin Poly(-methylmethacrylate) LB Films for X-Ray High-Resolution Lithography"; MS received 7 Mar 93, revised 12 Apr 93]

[Text]

Abstract

This is the first report of research on X-ray lithography on Langmuir-Blodgett (LB) monomolecular layers as photoresists. Each layer is made by drawing at a force of 15 dynes/cm. The thickness of the photoresists made from PMMA LB layers varies from 1.8 nm to 6.3 nm. The exposure is made with a low-dose X-ray of 360 mA-min. A resolution of 0.2-0.3 μm is achieved. (The resolution is limited by the maximum resolution of the mask, which is 0.2-0.3 μm.) The potential of adopting LB films as photoresists to improve X-ray lithography resolution from submicron class to nanometer class is discussed.

Key words: X-ray lithography, Langmuir-Blodgett (LB) films, Resolution, Nanometer structure.

A crucial factor in developing optoelectronic devices is in the area of nanometer technology, including especially lithography and its technology. As the required lithography standards in line width and resolution have advanced from the micron to the submicron and even to the nanometer range, electron-beam lithography and X-ray lithography become more and more important. The consensus is that it costs less to lithograph the mask first and then duplicate the pattern in the mask onto the photoresist of the chip with X-rays, compared with engraving the pattern directly onto the photoresist of the chip with an electron beam. The former method will greatly increase the production rate.[1] Photoresist research has always been a very important link to X-ray lithography development. The resolution of X-ray lithography depends not only on such factors as X-ray wavelength, intensity, developing technique, and lithographic technique, but also on the resolution of the X-ray exposure on and the developing of the photoresist.[2]

R. Feber et al. have suggested an ideal photoresist model.[3] The X-rays are orthogonally projected onto a photoresist which is composed of a group of resolution elements. A resolution element is defined as the smallest volume element that can be resolved after the photoresist is developed. Its standard denotation is δ x δ for area, and d for thickness, as shown in Figure 1. In a unit time period, the average dose of X-rays absorbed by each resolution element is expressed by the following equation:

$$\dot{\varepsilon} = \frac{Einc}{H\nu} \cdot A \cdot \delta^2 \qquad (1)$$

where Einc is the exposure intensity; Hv, the energy of every X-ray quantum; and A, the energy absorption rate of a unit photoresist area with thickness d. Assuming that the linear absorption coefficient is α, then A is expressed as:

$$A = 1 - e^{-\alpha d} \qquad (2a)$$

$$A \approx \alpha d \text{ (when } \alpha d << 1) \qquad (2b)$$

The factor limiting the X-ray photoresist resolution is

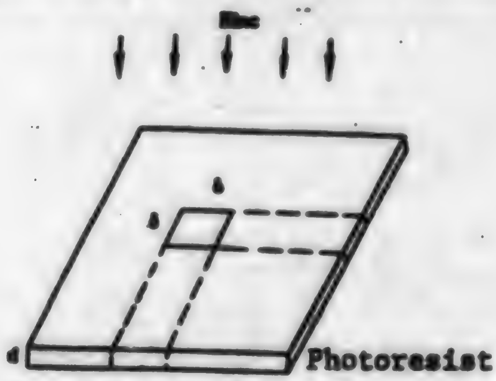

Figure 1. Resolution Element in Photoresist

dimension δ of the effective zone which can generate secondary electrons. The secondary electrons are the main motive force causing practically all the occurrences of the chemical reactions.[4] According to research results of E. Spiller et al., to improve the resolution to the maximum (δ → λ), the photoresist must be very thin, i.e.,

$d \approx \delta$.[5] Let us assume $d = \delta$; substituting the value into Equations (2b) and (1), we obtain:

$$Einc = \frac{\bar{n} \cdot h\nu}{\alpha \cdot \delta^3} \qquad (3)$$

We can see from the above that an ideal high-resolution photoresist should have low sensitivity. This requirement can also be applied to lithography in the micron and nanometer classes. As far as high-resolution photoresists are concerned, while the level of radiation remains unchanged, the process must be done under the condition of using corresponding ultrathin films. Based on this model, R. Feber et al. exposed PMMA photoresists with $d \approx 50$ Angstroms under the conditions $\lambda = 44.8$ Angstroms, $\bar{n} = 1.4$. They produced microscopic photographs of patterns with a nearly 50 Angstrom resolution in the nanometer class.[3]

Currently, photoresists are mainly made by the spinning method or the spray method. When making films of less than 50-nm thickness, these methods have the drawbacks of non-uniform thickness and high defect density; however, films of uniform thickness and considerably low defect density can be made with the LB film technique.[6] The technique is as follows: An organic material or polymer solution is spread on a sub-phase (e.g., water, glycerin, etc.) to form a monomolecular layer on the liquid surface. The layer is then transferred one after another onto a substrate and forms a solid ultrathin film with ordered molecular arrangement. Recently, many electron-beam photoresists have been made with LB films.[6,8] The LB film has definite future application in eliminating the "proximity effect" of the electron beam as well as producing nanoscale lithography patterns.[9]

The process to prepare LB films from poly(methylmethacrylate) or PMMA is as follows: First, the PMMA powder of molecular weight 1.8×10^5 (made by Huajin Company in Wuxi) is dissolved in trichloromethane ($CHCl_3$) forming a 0.5 mg/ml PMMA/$CHCl_3$ solution. The stable pure-water sub-phase in the Langmuir trough is made of super-pure water, twice distilled de-ionized water having electrical conductivity no higher than 10^{-8} $(\text{ohm-cm})^{-1}$. The Langmuir trough is of the FACE type (made by Kyowa Kaimenkagaku Co. Ltd.). The PMMA/$CHCl_3$ solution is spread and forms a monomolecular layer on the sub-phase liquid. Figure 2 shows the curve plotted from the data of layer pressure and layer area (π - A). It reveals that PMMA forms a gas layer on the sub-phase liquid surface when the pressure is 2 dynes/cm; when the pressure is between 2 dynes/cm and 12 dynes/cm, the layer gradually transforms to a hybrid gas-liquid state. These properties are highly in line with the experimental results by Kuan et al.[10] Stoveve observes that when the film pressure is about 15 dynes/cm, the PMMA main chain is basically parallel to the gas-liquid interface and densely arranged on the liquid surface.[11] Hence, when we transfer the PMMA solid film to the substrate, we always maintain the pressure at 15 dynes/cm.

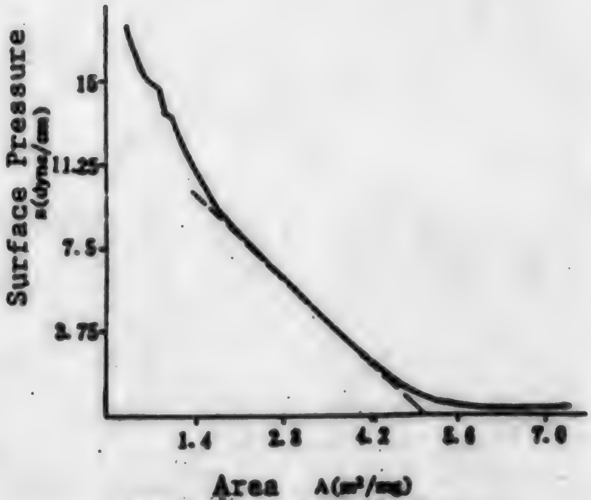

Figure 2. π - A of PMMA Curve

Pressure temperature, 14°C; PMMA molecular weight, 1.8×10^5

The chemically cleaned and hydrophobically treated Si chip is attached on the film extractor. The layer first extracted is baked at 100°C for 20 minutes to improve its adhesiveness to the chip; after that the extracting process is conducted in a continuous and vertical manner. After every 10 layers (up and down five times each way), the assembly is baked at 100°C for 10 minutes. Every PMMA layer is about 0.9 nm thick,[12] therefore the total thickness of the PMMA LB film transferred to the chip is the product of 0.9 nm and the number of layers. In the experiment under discussion, the total thickness of the PMMA LB photoresist for X-ray exposure is in the range of 1.8-6.3 nm.

The X-ray lithography test was conducted on the Si chips with PMMA LB films. The X-ray source is from the photolithography station of the synchrotron radiation accelerator in the State Synchrotron Radiation Laboratory operated by the University of Science and Technology of China. The wavelength of the X-rays ranges from 5 to 15 Angstroms; after filtering, from 5 to 10 Angstroms. The exposure area is 40 x 20 mm. The dose intensity is calculated as the product of accelerator tube current and exposure time, not counting the decaying current. Only one X-ray mask is used in the experiment. The maximum resolution is 0.2-0.3 μm (France). The developer is MIBK: IPA = 3:1 (20°C).

The X-ray exposure test shows that in the case of a PMMA LB film of about 36 to 63 nm thickness and 40 to 70 layers, good image quality can be achieved with an X-ray dose of 250 to 360 mA-min. The maximum mask resolution can be reproduced. In the case of a conventional film thicker than 1 μm made by the spinning method, an X-ray dose of 500 to 700 mA-min is needed for a quality image. Figure 3 shows three sets of grating images by a scanning electron microscope. Figure 3b

shows the recurrence of the 0.2 to 0.3-μm maximum mask resolution. Figure 4 shows a different mask pattern, which is a checkerboard pattern developed after the X-ray exposure. Because the developer solution is too strong, the first 20-layer PMMA LB film does not reveal any image. Besides, any dose over 400 mA-min is also not suited for PMMA LB films with fewer than 70 layers.

Figure 3. SEM Photo of X-Ray Lithograph on PMMA LB Photoresist (a) Gratings of 3 different resolutions; (b) Resolution: 0.2 to 0.3 μm

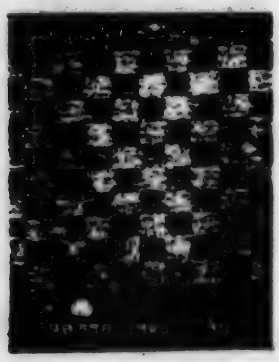

Figure 4. Developed SEM Photo of X-Ray Exposed PMMA LB Photoresist (checkerboard pattern)

Since lithography results depend also on other factors such as the composition of developer, the exposure time and other post-treatment techniques, the findings of this experiment, merely the results of our first trial, are deemed as preliminary; however, the experiment shows that there is a valid potential of making X-ray photoresists with LB films. The fact that the resolutions of the films progress from the micron to the submicron range, even to the nanometer range is especially important. Moreover, for the same resolution, employing the LB film can lessen the X-ray equipment requirement, e.g., reducing the demand on X-ray power, and eventually cutting down the cost. To overcome the problem wherein a thinner film leads to a weakening of the photoresist, concrete technology may consider utilizing different resolutions and photoresist materials of varying film thickness to produce photoresists through the LB or other techniques. Another method to improve the photoresist property is to have the exposed photoresist layer undergo the self-rearranging growth measure. Further work on the project is now in progress.

References

1. Herriot, D. R., et al., IEEE TRANS., ED-22, 1975:385.
2. Dagneaux, P., et al., ANN. PHYS (Paris), 1975, 9:9.
3. Feder, R., et al., SCIENCE, 1977, 197:259.
4. Spear, D. L., et al., ELECTRON LETTERS, 1972, 8:102.
5. Queisser, H.-J., "X-Ray Optics, Applications to Solids," Springer-Verlag, 1977.
6. Barraud, A., et al., THIN SOLID FILMS, 1980, 68:91.
7. Hupfer, B., et al., MAKROMOL. CHEM., 1981, 182:247.
8. Cemel, A., et al., J. POLYM. SCI., 1972, A1-10, 2061.
9. Gu Ning, et al., Proceedings of First Conference on Functional Materials, Guilin, 1992, 10.
10. Kuan, S. W. J., et al., J. VAC. SCI. TECH., 1988, B5(6):2274.
11. Stroeve, P., et al., THIN SOLID FILMS, 1987, 146:209.
12. Zhang, H., et al., J. VAC. SCI. TECHNO., 1989, B7(6):1717.

More Reports on Nanomaterials

Preparation, Optical Properties of Cu_2O Nanocrystals

94FE0161A Beijing KEXUE TONGBAO [CHINESE SCIENCE BULLETIN] in Chinese Vol 38 No 18, 16-30 Sep 93 pp 1649-1651

[Article by Zou Bingsuo [6760 3521 6956], Tang Guoqing [3282 0948 1987], Zhang Guilan [1728 2710 5695], and Chen Wenju [7115 2429 7467] of the Institute of Modern Optics, Nankai University, Tianjin, 300071, and Li Tiejin [2621 6993 3160], Zhang Yan [1728 1484], and Xiao Liangzhi [5135 5328 6347] of the Department of Chemistry, Jilin University, Changchun, 130023: "Preparation and Optical Properties of Cu_2O Nanoparticles," funded by the Natural Science Foundation of China and the Post-Doctoral Foundation of the State Education Commission; MS received 5 Nov 92, revised 1 Mar 93]

[Text] Key words: Cuprous oxide, nanoscale particles, preparation, exciton limitation, optical characteristics.

Due to the quantum confinement effect, semiconducting nanoparticles produce a series of new phenomena,[1,2] among which the materials with ultrafast optical nonlinear response have been particularly noticed. It is predicted that these semiconducting materials will be the basic optoelectronic materials of the future. The study of the opto-absorption and -relaxation properties of nanoscale crystals will help us further understand the mechanism of nonlinear optical response.

When the size of a semiconducting nanocrystal is as small as the Bohr radius a_B of its own phase, a series of changes of electronic state and optical property can be observed. These phenomena are observed in the semiconducting nanocrystal systems of CdS, CuCl, CdSe, PbS.[3,4] The ratio of the nanocrystal radius R to its Bohr radius a_B can be used as the general guideline to determine the influence of the quantum confinement effect on the electronic state:[5] When $R/a_B << 1$, the nanoparticles are in the strong quantum confinement zone, and their energy levels of electrons and holes are clearly separated; however, when $R/a_B >> 1$, the nanocrystal is in the exciton confinement zone where the excitons act as quasi-particles whose translation kinetic energy's degree of freedom is confined within the three-dimensional space; as a result the exciton energy increase is limited. Currently, only CuCl nanocrystals are being researched as an exciton-confinement-zone material, and they are also good model materials for the study of excitonic molecule properties. This paper presents the preparation of cuprous oxide (Cu_2O) nanocrystals and discussion of their optical properties, as well as a discussion of results based on the model of exciton responses to the quantum confinement effect.

1. Experiment

The Cu_2O nanocrystals are made by the oxidation-reduction method in a micro-emulsive liquid. The process flow diagram is as follows:

The Cu_2O nanocrystals made by this method are all coated with sodium dodecylbenzene sulfonate (DBS) molecules, and form a transparent sol with toluene. The crystal sizes can vary within the limit of 5-10.0 nm as determined by the initial value of $[CuAc_2]/[DBS]$. The transmission electron microscope and the low-angle X-ray scattering experiments show that the spread of the Cu_2O nanocrystal dimensions is very narrow. About 93 percent of the crystal dimensions have the median radius, and the rest are distributed within the 10 percent of the median radius. The radius distribution of the nanocrystals is thus well suited for the study of optical properties.

The room-temperature photoluminescence and excitation spectra of the Cu_2O nanocrystal sol series are measured with a Hitachi F-4000 fluorescence spectrometer.

2. Results and Discussions

The visible-ultraviolet absorption spectra of Cu_2O nanocrystal (9.0 nm) organic sol starts at 650 nm. The absorption rate gradually increases toward the high-frequency region, but there is no clear indication of

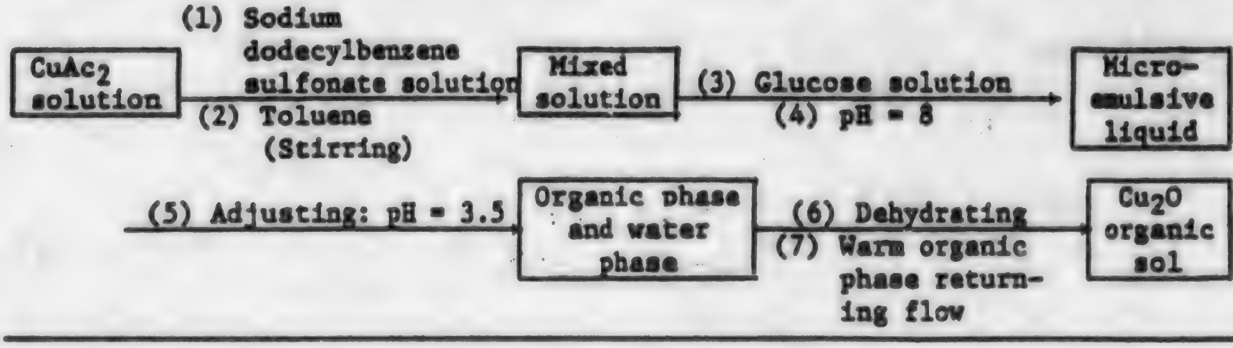

structural absorption characteristics. This implies that the phenomenon is influenced by two factors: one is the temperature and solvent effects; and the other is the size effect. Because the dimensions of the nanocrystal are far greater than the Bohr radius a_B (0.7 nm) of its own phase, the increase of the exciton energy is not obvious, and the energy separation induced by the confinement effect is very minor.

Figure 1 shows the photoluminescence spectra of the Cu_2O nanocrystals. The excitation luminescences are (1) 330 nm, (2) 400 nm, (3) 440 nm, (4) 460 nm, (5) 510 nm, and (6) 532 nm. Five luminescence bands are visible in the neighborhood of 400 nm, 475 nm, 505 nm, 540 nm and 565 nm. The last four bands correspond to the existing four luminescence bands in the exciton systems, namely, indigo, blue, green, and yellow.[6] The energy changes in the exciton confinement zone are comparatively small. The luminescences are undoubtedly fluorescence resonance emissions. In addition, the luminescence at 400 nm indicates the presence of energy jumps between bands within the Cu_2O crystal. The emission luminescence has not been reported in the past, but its absorption structure was reported long ago.[7] The emission from the bottom of the conduction band in the exciton confinement zone possibly originates from the bound excitons formed at the bottom of the band; however, further proof is needed. As to the luminescence phenomenon of solids at high energy level (or energy band), it is rarely seen in solid-state phases and many other nanocrystals. However, in our research we have observed that the phenomenon of increasing high energy-level radiation jumps not only takes place in the aforementioned Cu_2O nanocrystals, but could also occur in the coated CdS and PbS nanocrystals. It is quite likely that in the high energy-level neighborhoods of the quantum confinement and dielectric confinement zones, stable bound excitons are formed, and consequently, they reduce the non-radiation jumping probability of the electrons or holes due to vibrations or impurities; thus, they enhance the radiation jumping. The phenomenon deserves further probing, because it has direct bearing on the enhancement of the system's nonlinear optical phenomena.

Figure 2 shows the excitation spectra of Cu_2O nanocrystal (0.9 nm) emission at (a) 600 nm and (b) 580 nm. They are equivalent to the exciton wavelength absorption structure.[6] Figure 2 shows the exciton jumps in the indigo, blue, green, and yellow series are all mutually related,[6] and have an obvious relationship with the jump at about 380 nm. There is a corresponding spectral region of each individual series, and occasionally these spectral regions overlap. The relatively low vibrator absorption intensities of the yellow and green exciton series are caused by the dipole forbiddenness of the jump.[9]

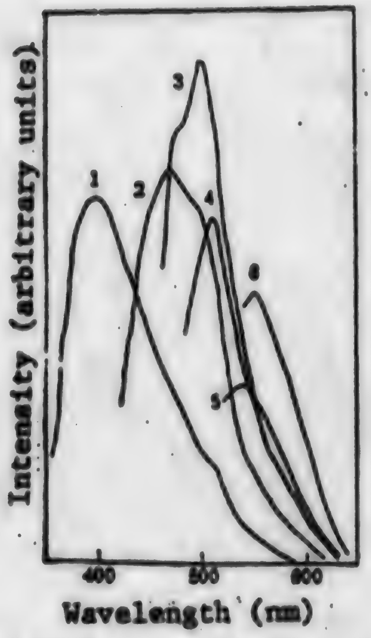

Figure 1. Photoluminescence Spectrum of Cu_2O Nanocrystal (9.9 nm) Sol

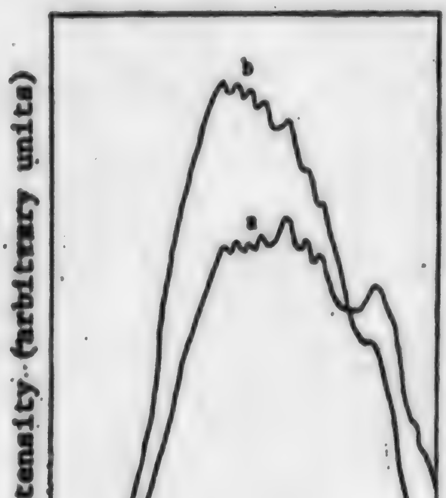

Figure 2. Excitation Spectrum of Cu_2 Nanocrystal (9.0 nm) Sol

a. 600 nm emission; b. 580 nm emission

Another interesting phenomenon in the excitation spectra is that the dipoles allow the indigo and blue exciton series having the multi-peak structures of jumps. Such structures are caused by the quantization of the exciton energy which in turn is due to the spatial quantum confinement effect.[10] Hanamura[2] has suggested a simplified mode. He assumes the exciton to be a quasi-particle situated in a semiconducting nanosphere; when $R/a_B >> 1$, the exciton energy ($l = m = 0$) that allows jumps is expressed as

$$E_n = E_0 - E^b_{ex} + n^2 E_c \qquad (1)$$

where E_c is the quantum confinement energy ($h^2\pi^2/2 M R^2$) and E^b_{ex} is the exciton bonding energy which varies with exciton's principal quantum number. The quantization of excitons follows the equation $E^b_{ex} = E_y/n^2$, where E_R is the effective exciton Rydberg energy ($\mu e^4/2h^2\epsilon^2_0$), $M = m_e + m_h$, $\mu = m_e m_h/m_e + m_h$, and hence the equation

$$E_n = E_0 - E_y/n^2 + n^2 E_c \qquad (2)$$

is used to describe the different exciton jumps with different principal quantum numbers in the same series. Our test results as shown in Figure 2 and Table 1 have proved the validity of Equation (2).

Table 1. Theoretical Value and Experimental Values of Indigo Exciton Jump

Experimental value ($R = 4.5$ nm, $a_B = 0.7$ nm)	Calculated value ($R = 4.35$ nm, $E_c = 146{,}413$ nm, $E_g = 12{,}407$ nm)
$E_1 = 468.2$	468
$E_2 = 451$	451
$E_3 = 438$	441.9
$E_4 = 428.8$	432.1
$E_5 = 420.6$	420.6

The aforementioned results demonstrate that the conclusion that the exciton energy increase in the exciton confinement zone is limited is valid only for the energy jump when $n = 1$. When $n \geq 2$, the blue shift of the jump is relatively significant. In this case, exciton jumps of different principal quantum numbers split away from one another, while the nanocrystal optical nonlinear response produces mesoscopic strengthening.[2] This phenomenon will benefit our study of mutual reactions among the excitons within the exciton confinement zone, such as the superradiation phenomenon.[1),11] Thorough research on the above phenomenon would be very worthwhile.

Acknowledgment: The authors are grateful to Professor Zhang Guangyin for his valuable papers and beneficial discussions.

1) Zou Bingsuo, Ph. D. Thesis, Jilin University, 1991.

References

1. Brus, L. E., APPL. PHYS., A, 1991, 53: 465-474.

2. Hananura, E., PHYS. REV., B, 1987, 37: 1273-1278.

3. Li Shoutian, et al., GAODENG XUEXIAO HUAXUE XUEBAO [HIGHER EDUCATION CHEMICAL JOURNAL], 1991, 12: 1393-1395 [in Chinese].

4. Kayanuma, Y., et al., APPL. PHYS., A, 1991, 53: 475-479.

5. Efros, Al. L., et al., SOV. PHYS. SEMICOND., 1982, 16: 772-774.

6. Hanamura, E., "Excitonic Processes in Solids," Springer-Verlag, Berlin, 1986, 46-47.

7. Zhang Guangyin, et al., WULI XUEBAO [ACTA PHYSICA SINICA], 1965, 21: 324-328 [in Chinese].

8. Kang, K. I., et al., PHYS. REV., B, 1992, 45: 3465-3468.

9. Agekyan, U. T., PHYS. STAT. SOL., (a), 1977, 43: 11-29.

10. Kayanuma, Y., PHYS. REV., B, 1988, 38: 9797-9805.

11. Itoh, T., et al., NONLIN. OPT., 1991, 1: 61-69.

Preparation of β-SiC Ultrafine Powder From Polysilane by CVD

93FE0226A Beijing GUISUANYAN XUEBAO [JOURNAL OF THE CHINESE CERAMICS SOCIETY] in Chinese Vol 21 No 5, Oct 93 pp 466-470

[Article by Zhang Changrui [1728 7022 3843] (correspondent), Chen Zhaohui [7115 2600 6540], Yan Dong [0917 0392], Song Yongcai [1345 3057 2088], and Chen Ge [7155 7245] of the Department of Materials and Applied Chemistry, National University of Defense Technology, Changsha, 410073: "Preparation of β-SiC Ultrafine Powder From Low-Molecular Polysilane by CVD"; MS received 12 Dec 91]

[Text]

Abstract

SiC ultrafine powder is prepared by the CVD [chemical vapor deposition] method using low-molecular polysilane as precursor and argon as carrying gas. The relationships between the powder properties and the preparation factors such as reaction temperature, carrying-gas flow rate, and reactant densities are studied. The β-SiC ultrafine powder with uniform size (< 0.1 μm), high purity (30 weight percent of carbon content),

and homogeneous crystalline structure is obtained through the decarbonization, deoxidization, and crystallization processes.

Key words: ultrafine silicon-carbide powder, CVD, low-molecular polysilane.

1. Introduction

Due to its high-temperature mechanical properties, and good thermal shock-resistance property, SiC is one of the major materials in research on using high-temperature ceramics for engine parts.[1]

To make superior ceramics by a sintering method, one of the crucial techniques is to prepare ultrafine (nanoscale) ceramic powders having the properties of non-agglomeration, size uniformity, and high purity.[2] The best method to prepare SiC ultrafine powder is the chemical vapor deposition (CVD) method.[3]

Among the several CVD methods, one is to prepare the SiC ultrafine powder from reactions between silicon-content monomers (e.g., $SiCl_4$, SiH_4) and carbon-content monomers (e.g., CH_4, C_2H_4),[4]; and another, from the thermal decomposition of organic silicon compounds containing both carbon and silicon (e.g., CH_3SiCl_3, CH_3SiH_3, $[(CH_3)_2Si]_3$, etc.).[3,5] However, in the monomer reactions, the existence of chlorine reduces the production rate, corrodes the equipment, and pollutes the environment. Moreover, when the carbon-to-silicon ratio (C/Si) is too low, too much free silicon is produced. Therefore, it is worthwhile to research other systems.

This paper studies the production factors of making SiC ultrafine powder from low-molecular polysilane (LPS), which is a by-product from synthesizing polyalkyl silane, as raw material and high-purity argon as carrying gas. The research also analyzes the composition, structure, and configuration of the ultrafine powder.

2. Experimental Work

2.1 Raw Materials: LPS is a by-product generated from the cracking process of making polyalkyl silane from polysilane. It is a pale yellow liquid composed of organic silicon oligomers with different boiling points. These oligomers have chain or ring structures with

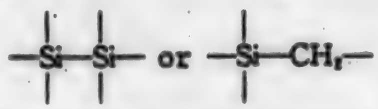

as the backbones, and an average molecular weight of 250. They vaporize completely at 300°C.

2.2 Carrying Gas: The carrying gas is high-purity argon with 12 x 10^{-6} of oxygen and 16.5 x 10^{-6} of H_2O as analyzed with a DH-3C trace-oxygen analyzer and a US-1-1A trace-water analyzer, respectively.

2.3 Apparatus for Preparation of SiC Ultrafine Powder: As shown in Figure 1.

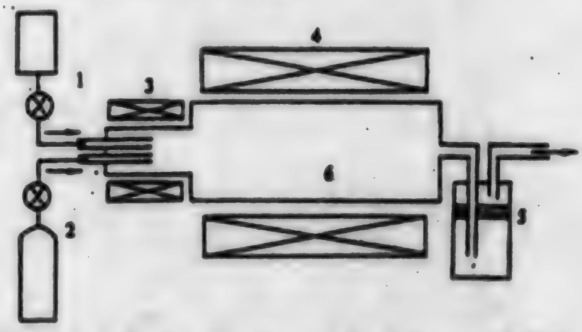

Figure 1. Schematic Diagram of the Apparatus for Preparation of SiC Ultrafine Powder

1. LPS and flowmeter; 2. Carrying gas and flowmeter; 3. Vaporizer; 4. Furnace; 5. Powder collector; 6. Pyrolysis tube

2.4 Decarbonization, Deoxidization and Crystallization of the Ultrafine Powder: The SiC ultrafine-powder product from the reaction is amorphous. The powder is treated at 1600°C for crystallization as well as decarbonization and deoxidization to remove the free carbon and oxygen in the ultrafine powder.

2.5 Ultrafine Powder Characteristics: The powder's infrared spectrum is obtained with a Hitachi 270-30 infrared spectrometer. The size and configuration of the powder are determined with a Hitachi H-800 transmission electron microscope (TEM); the powder crystal structure, with a type D/max-IIIA X-ray diffractometer; and the carbon, hydrogen, and nitrogen contents, with a USA PE2400CHN element analyzer.

3. Results and Discussions

3.1 Effects of Reaction Temperature

Under the condition that the argon flow rate is controlled at 0.24 L/min; and LPS flow rate, 0.025 g/min, different powder batches are made within the temperature range of 900 to 1300°C, as shown in the TEM photos in Figure 2. The reaction temperature has little effect on the particle size and configuration. The powder diameters are between 0.05 and 0.1 μm with very narrow distribution, and most particles are spherical.

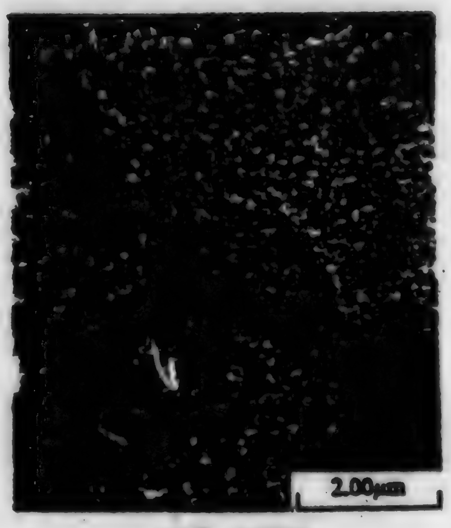

(a) T_m = 900℃

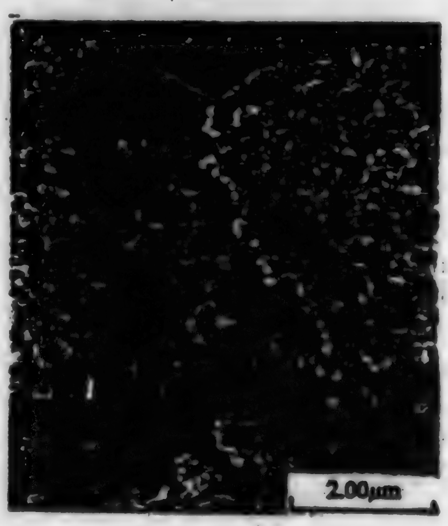

(b) T_m = 1300℃

Figure 2. SEM Photographs of SiC Powder Synthesized at Different Temperatures

Ar: 0.24 L/min; LPS: 0.025 g/min; Vaporizer temperature: 200°C

Figure 3 shows the relationship between the powder's carbon and the hydrogen contents and the reaction temperature. The carbon content increases and the hydrogen content decreases with the increase of the reaction temperature. The fact that the hydrogen content in the SiC product is zero at the reaction temperature 1300°C indicates that the transformation of the organic LPS to the inorganic SiC is complete. In LPS, the ratio of carbon to silicon is 2:1, therefore the total carbon content in the ultrafine powder exceeds the theoretical value (30 weight percent) and free carbon exists in the final product. At low temperature, the main cracking product is CH_4 which will be carried out by the gas flow; as a result, the carbon content is comparatively low for the low-temperature reaction product. At high temperature, the cracking product is mainly H_2, therefore the free-carbon content in the product increases.

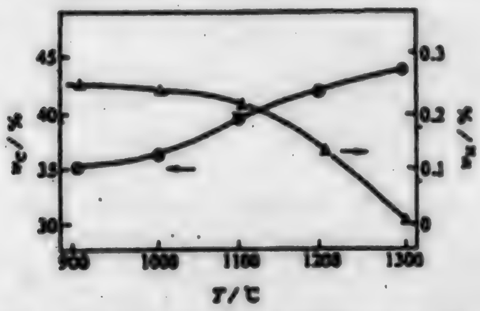

Figure 3. Effect of Reaction Temperature on the C and H Mass Content in SiC Powder

Figure 4 depicts the infrared spectra of products obtained at different temperatures. It shows that as the temperature increases, the transformation of the organic LPS to the inorganic SiC is gradually completed. At 450 cm^{-1}, there is a Si-O absorption peak. As the temperature increases, the peak becomes weaker. The existence of the Si-O bond is caused by the infusion of oxygen, one of the impurities in LPS.

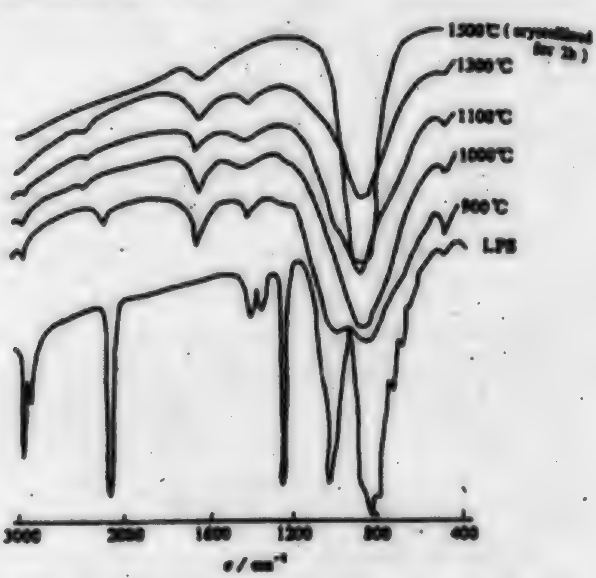

Figure 4. Infrared Spectra of LPS and Its Pyrolytic Products Obtained at Different Reaction Temperatures

3.2 Effects of Carrying-Gas Flow Rate

When the reaction temperature is controlled at 1100°C and LPS flow rate at 0.025 g/min, at different argon flow

rates, the ultrafine powders remain spherical. When the argon flow rates are 0.088 L/min, 0.24 L/min, and 0.535 L/min, the diameters of the ultrafine powder are 0.1 μm, 0.075 μm, and 0.04 μm, respectively. The SiC ultrafine-powder diameter decreases with an increase in the argon flow rate. The SiC ultrafine-powder growth is a kinetics phenomenon. After SiC ultrafine powder is formed, its growth depends on its length of stay in the furnace. The higher the carrying-gas flow rate, the shorter the SiC's stay in the furnace, consequently the finer the powder produced.

3.3 Effects of LPS Flow Rate

When the furnace temperature is controlled at 1100°C and argon flow rate at 0.24 L/min, SiC ultrafine powders are prepared at different LPS flow rates. The results show that when the LPS flow rate is at 0.025, 0.065, or 0.160 g/min, all powders are spherical having a diameter 0.75 μm, which indicates that the LPS flow rate does not affect the size or the configuration of the SiC ultrafine powder.

3.4 Decarbonization, Deoxidization, and Crystallization of SiC Ultrafine Powder

As aforementioned, the SiC ultrafine powder prepared by this method contains free carbon and SiO_2, which as impurities produce unfavorable effects on the material; thus, decarbonization and deoxidization are needed. Besides, the prepared SiC ultrafine powder is amorphous, therefore, crystallization is also needed.

To achieve the purpose of decarbonization and deoxidization and in the meantime crystallization, this process utilizes high-temperature (about 1500°C) reaction in which free carbon reduces SiO_2 and forms gaseous SiO and CO, which eventually evaporate. At the same time the crystallization is also completed. The XRD results (Figure 5) show that as the crystallization temperature increases, the SiC ultrafine powder gradually transforms from the amorphous state to the β-SiC crystalline state. When the reaction temperature reaches 1500°C, β-SiC is virtually completely crystallized, and no other phases are observed.

Figure 4 shows that after crystallization for 2 hours at 1500°C, the infrared absorption peak at 450 cm^{-1} in the SiC ultrafine-powder spectrum disappears, which indicates that the powder is deoxidized.

The element analysis shows that the carbon content of decarbonized SiC drops from 39.54 percent to 30.15 percent, which is basically close to the theoretical carbon content (30 percent) of SiC. The fact that the color of the ultrafine powder changes from brownish to whitish also indicates that the powder is completely decarbonized.

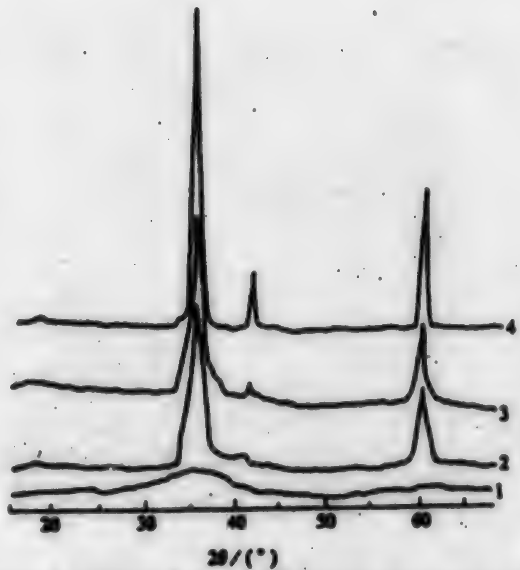

Figure 5. XRD Patterns of SiC Powder Treated at Different Temperatures

1. Not treated; 2. 1380°C; 3. 1450°C; 4. 1500°C

4. Conclusions

(1) The LPS CVD technique can produce SiC ultrafine powder. The technique is feasible because of its low processing temperature, lack of corrosion, and simple procedures.

(2) The carbon and hydrogen contents are mainly controlled by the reaction temperatures: the higher the reaction temperature, the higher the carbon content, and the lower the hydrogen content. The SiC ultrafine-powder size is controlled by the carrying-gas flow rate: the higher the flow rate, the smaller the particle size.

(3) After the transformation from LPS, the SiC powder product is always carbon rich. After the decarbonization, deoxidization, and crystallization treatment, high-purity, uniform-sized and almost completely crystallized spherical β-SiC ultrafine powder can be obtained.

References

1. Johnson, D. R., "Ceramic Technology for Advanced Heat Engines Project," DOE DE88008945, Washington, DC: DOE, 1988.

2. Chen, L. D., Goto, T., Hirai, T., "Preparation of Silicon Carbide Powders by CVD of the $(CH_3)_2SiCl_2$-H_2 System," J. MATER. SCI., 1990; 25: 4614.

3. Chen, L. D., Goto, T., Hirai, T., "Preparation of Silicon Carbide Powders by CVD of the SiH_4-CH_4-H_2 System," J. MATER. SCI., 1989; 24: 3824.

4. Cannon, W. R., Danforth, S. C., Flint, J. H., et al., "Sinterable Ceramic Powders From Laser-Driven Reaction," J. AM. CERAM. SOC., 1982; 65: 324.

5. Tanaka, H., Kurachi, Y., "Synthesis of β-SiC Powder From Organic Precursor and Its Sinterability," CERAM. INT., 1984; 14: 109.

STM Research on Nanoscale Si Thin Films

94FE0226B Beijing KEXUE TONGBAO [CHINESE SCIENCE BULLETIN] in Chinese Vol 38 No 21, 1-15 Nov 93 pp 1953-1955

[Article by Wang Zhonghuai [3769 1813 2037], Dai Changchun [2071 7022 2504], Zhang Pingcheng [1728 1627 1004], and Bai Chunli [4101 2504 4409] of the Institute of Chemistry of the Chinese Academy of Sciences (CAS), Beijing 100080, and He Yuliang [0149 1342 0081] of the Amorphous-State Research Section, Beijing University of Aeronautics and Astronautics, Beijing 100083: "Study on STM Research on Nanoscale Si Thin Film," funded by NSFC and the CAS Major Projects Fund; MS received 19 Mar 93, revised 3 Jul 93]

[Text] Nanoscale Si thin film (nc-Si:H) is a nanoscale material composed of nanoscale ultrafine crystals.[1,2] The material contains 50 volume percent of crystals, and the other 50 percent contains a large number of interface atoms which greatly affect the structure and the property of the nanoscale material.[3] Because of the novelty of the nanoscale Si thin-film structures, the film has a series of special characteristics that are different from crystalline or amorphous materials made of similar substances. These optical characteristics present application potential.[4,5]

The scanning tunneling microscope (STM) developed in the early 1980s has been widely used in different fields.[6,7] The study of polycrystalline Si thin film with STM has achieved some results,[8-11] mainly in the exploration of the film's surface characteristics and topography. However, so far there has been no report of STM research on the nanoscale material's crystal interface, which has an important effect on the structure and properties of the nanoscale material. In this paper, we utilize a locally made STM to study the surfaces of nanoscale Si thin films whose thickness varies from sub-micron to atomic scale. A series of data, especially on the crystal interface structures, is obtained.

1. Experimental Method

The nanoscale Si thin-film specimen is prepared with a plasma capacitively coupled chemical vapor deposition (PECVD) system, with highly hydrogen-diluted silane as the reaction gas, and by the excitation of an r.f. +DC double-power source.[1,2]

The instrument used in the research is a type CSTM-9000 STM for atmospheric use,[12] manufactured by the CAS Institute of Chemistry and equipped with a needle made of 80Pt-20Ir alloy (diameter: 0.25mm) by mechanical cutting or a tungsten needle (diameter: 0.25mm) made by chemical etching. In a constant-current operating mode, each image is sampled with 180 x 180 points. The surface heights are reflected by the varying shades of grayish color in the image. The voltage between the needle and the specimen tunnel junction is between 0.5 V and 2 V, with needle as positive. The maximum tunnel current selected for use has reached 1 nA, and generally is about 0.5 nA. In the following test results, the STM images are only the outcomes after the original data were smoothed. The scanning time for each image varies: from 3 min (for large images) to 15 s (for small images).

2. Results and Discussion

The STM images of nanoscale Si thin film of different magnifications in atmosphere are displayed from sub-micron to atomic dimensions. Figure 1 shows the obverse STM image of the nanoscale Si thin film obtained with the tungsten needle. The needle bias is 1 volt; and the current, 0.45 nA. The scanning areas of Figures 1(a) and 1(b) are 40.9 nm (x-direction) x 48.8 nm (y-direction), and 20.5 nm x 24.4 nm, respectively. Figure 1 shows that the nanoscale Si thin film is composed of many ultrafine particles. The densities of the surface particle arrangements vary. The particle boundaries are very clear. From Figures 1(a), and 1(b) especially, the sizes of the nanoscale Si thin-film particles can be estimated as 3 nm-5 nm, which closely coincide with the results from high-resolution electron microscopy (HREM).[1,2] The image obtained with the mechanically cut Pt/Ir needle shows comparatively smooth regions between the nanoscale particles in the nanoscale Si thin film, due to the large radius of curvature of the mechanically cut Pt/Ir needle tip.[13] Figure 2 shows the three-dimensional STM near-atomic image of the nanoscale Si thin film obtained with the Pt/Ir needle. The STM parameters are: needle bias V_t =1.0 V; tunnel currents I_t are 0.4 nA and 0.6 nA for Figures 2(a) and 2(b), respectively; and the scanning areas are 4.10 nm x 4.88 nm and 1.7 nm x 1.0 nm, respectively. Figure 2(a) shows that the atoms in the brighter areas arrange in an orderly pattern, and the darker areas are the boundary surfaces of the crystals where the atom arrangements are somewhat random. This observation essentially coincides with Gleiter's

nanoscale material structural model.[3] Two scratch marks caused by the unstable needle are displayed in Figure 2(a). Figure 2(b) displays the orderly arrangement of atoms with a distance of about 3 Angstroms between neighboring atoms. At this position, we believe that the area of STM observation is focused on the particle. Since the particle is crystalline,[1,3] the orderly arrangement of the atoms is observable.

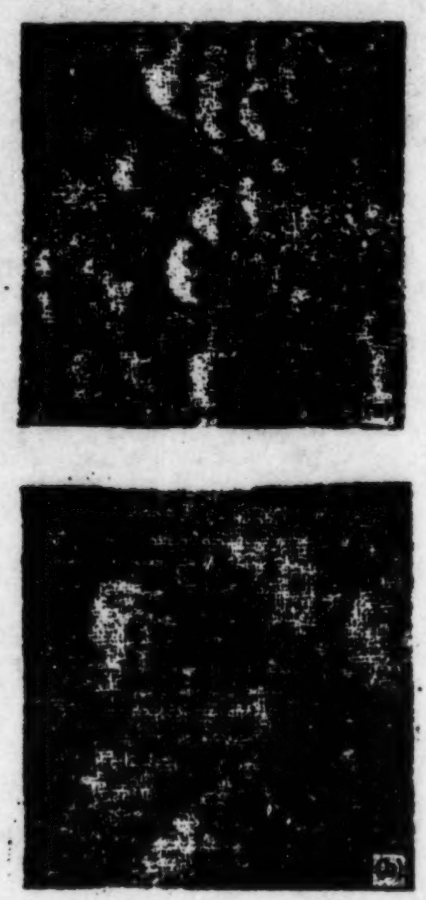

Figure 1. Plane Image of Nanoscale Si Thin Film
Scanning area: (a) 40.9 nm x 48.8 nm, (b) 20.5 nm x 24.4 nm

This experiment has found that the needle bias for image formation should not be too low to cause needle instability, which is probably due to the nanoscale Si thin-film surface oxidation. On the other hand, during the preparation of the nanoscale Si thin-film specimen, the reaction between silicon and hydrogen may hinder the surface oxidation. These results are only preliminary. Further study is in progress.

3. Conclusions

The STM study of nanoscale Si thin film reveals that this film is composed of nanoscale particles with

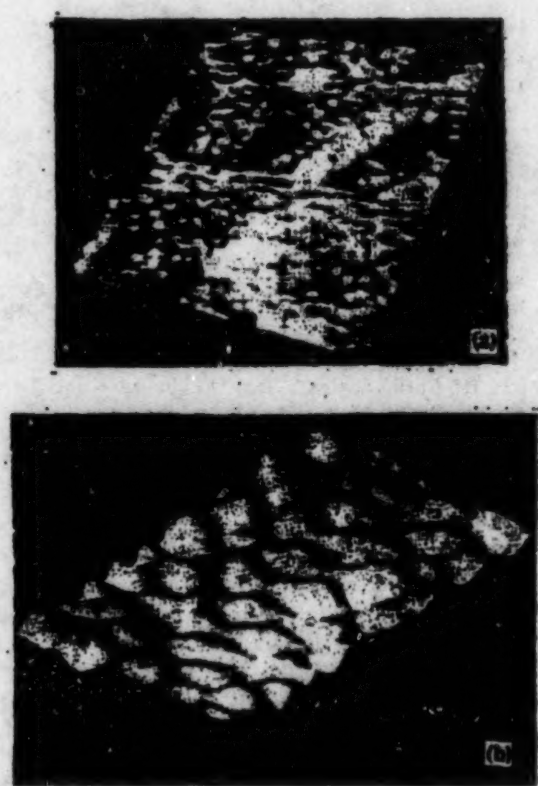

Figure 2. Three-Dimensional STM Near-Atomic Image of Nanoscale Si Thin Film
Scanning area: (a) 4.10 nm x 4.88 nm, (b) 1.7 nm x 1.0 nm

average particle size of 3 nm-5 nm. Through the STM's high-resolution imaging capability, the near-atomic images on the thin-film surface are directly observed. The images show that the atom arrangement of the nanoscale particles is orderly, and the atom arrangement between the particles is comparatively random. These results coincide with past observations by HREM, and further disclose the microstructure of the nanoscale Si thin film.

Acknowledgment: The authors are grateful to Research Fellow Xu Yiming and Senior Engineer He Liang of the CAS Institute of Semiconductors and to Professor Lin Hongyi of Beijing Institute of Technology for their enlightening discussions.

References

1. He Yuliang, Yin Chenzhong, Cheng Guangxu, et al., BANDAOTI XUEBAO [CHINESE JOURNAL OF SEMICONDUCTORS], 1992, 13(11): 683-689 [English abstract in JPRS-CST-93-001, 7 Jan 93 p 35].

2. He Yuliang, Liu Xiangna, Wang Zhichao, et al., ZHONGGUO KEXUE, Series A, 1992, (9): 995-1001 [abstracted in JPRS-CST-93-001, 7 Jan 93 p 7].

3. Gleiter, H., EUROPHYSICS NEWS, 1989, 20(9): 130-133.

4. Zook, J. D., APPL. PHYS. LETT., 1980, 37(2): 223-226.

5. Ashburn, P., Soerowirdjo, B., IEEE TRANS. ELECTRON DEVICES, 1984, Ed-31, 853-860.

6. Bai Chunli, ed., "Scanning Tunneling Microscopy and Its Applications," Shanghai Science and Technology Press, 1992 [in Chinese].

7. Wang Zhonghuai, Dai Changchun, Sun Hong, et al., KEXUE TONGBAO [CHINESE SCIENCE BULLETIN], 1993, 38(5): 433-435 [translated in full in JPRS-CST-93-013, 27 Jul 93 pp 10-11].

8. Gimzewski, J. K., Humbert, A., Pohl, D. W., SURFACE SCIENCE, 1986, 168: 795-800.

9. Hosaka, S., Sagara, K., Hasegawa, T., et al., J. VAC. SCI. TECHNOL., 1990, A8(1): 270-274.

10. Carrejo, J. P., Thundat, T., Nagahara, L. A., et al., J. VAC. SCI. TECHNOL., 1991, E9(2): 955-959.

11. Sugawara, Y., Fukano, Y., Kamihara, Y., et al., ULTRAMICROSCOPY, 1992, 42-44: 1372-1375.

12. ixBai Chunli, KEXUE TONGBAO [CHINESE SCIENCE BULLETIN], 1989, 34(5): 339-340.

13. Musselman, I. H., Russell, P. E., J. VAC. SCI. TECHNOL., 1990, A8(4): 3558-3562.

Raman Spectroscopy of Nanoscale SnO_2

94FE0226C Beijing KEXUE TONGBAO [CHINESE SCIENCE BULLETIN] in Chinese Vol 38 No 21, 1-15 Nov 93 pp 2014-2015

[Article by Zuo Jian [1563 1696], Xu Cunyi [6079 1317 5030], Liu Xianming [0491 0341 2494], and Wang Changsui [3769 2490 3606] of the Structural Analysis Open Laboratory, and Wang Chengyun [3769 2052 0061], Hu Yuan [5170 3293], and Qian Yitai [6929 6654 3141] of the Department of Applied Chemistry, University of Science and Technology of China (USTC), Hefei, 230026: "Study of Raman Spectroscopy of Nanoscale SnO_2," funded by NSFC and the USTC Structural Analysis Open Laboratory Foundation]

[Text] SnO_2 nanoscale crystal powder is prepared with a hot-water method as follows: The metallic tin powder is mixed with nitric acid and the reaction turns the mixture into a transparent solution. The solution is then mixed with polytetrafluoroethylene and loaded in an autoclave at 150°C for 24 hours. After the treated solution is cooled to room temperature, white SnO_2 powder is obtained. The powder is washed thoroughly, baked at 150°C for 24 hours, and then pressed into a plate under a pressure of 10^8 kg/cm^2. The initial particle size of the specimen is 3 nm. After annealing at different temperatures, nanoscale SnO_2 powders of different particle sizes are obtained. The powder crystal structure belongs to the rutile type, and there is less than 1 percent of impurities in the powder.

The Raman spectrum is measured with a U.S. SPEX-1403 laser Raman spectrometer. The excitation light is the 514.5-nm line from an argon-ion laser. The back-scatter configuration is adopted. All measurements are conducted at room temperature.

Figure 1 shows that the peaks in the Raman spectra are of two different groups: the peaks in one group, called mode A, correspond with the peaks in the monocrystalline or polycrystalline SnO_2 spectra. The Raman spectrum peaks with wave numbers of 472, 632, and 773 cm^{-1} are designated as A_1, A_2, and A_3, respectively. In the other group, called mode B, the peaks with wave numbers of 358 and 572 cm^{-1} are designated as B_1 and B_2, respectively. The mode-B peaks do not exist in the monocrystalline or polycrystalline SnO_2 Raman spectra. This observation indicates that the appearance of B_1 and B_2 peaks is caused by the nanoscale effect.

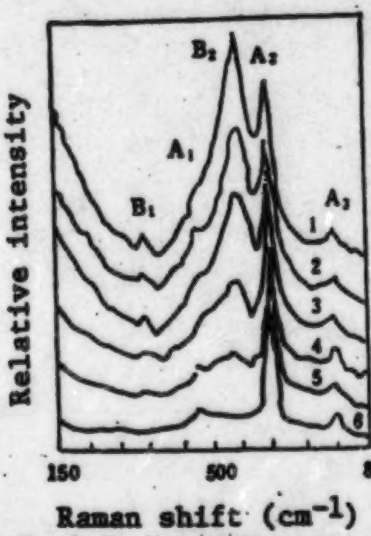

Figure 1. Raman Spectra of Different Nanoscale SnO_2 Solids

1-6 are 3, 4.4, 6.5, 9, 13, and 90 nm, respectively

All the peak intensities in Figure 1 are normalized according to the intensity of peak A_2. As shown in Figure 1, the intensity ratios of the peaks in mode B to the peaks in mode A increase rapidly with decrease in

crystal size. This observation is similar to the phenomenon wherein surface-atom fractions rapidly increase with decrease in crystal size. We assume that the B_1 and B_2 peaks are caused by the surface phonon modes and are closely related to the A_1 and A_2 peaks. This experiment shows that the frequencies of the B_1 and B_2 peaks are lower than those of the A_1 and A_2 peaks. The appearance of the low-frequency surface phonon modes is induced by the relaxation among the surface atoms. This relaxation weakens the interaction among the surface atoms, and consequently reduces the surface force coefficient.

Calculations based on the Raman spectra of nanoscale solid materials are expected to generate the specific positions of the nanoscale surface atoms.

Acknowledgment: The authors are grateful to Professors Qian Linzhao and Zhu Qingshi for their interest and guidance throughout this research.

- END -

END OF
FICHE
DATE FILMED
20 APR 1994